Single identified hadron spectra from $\sqrt{s_{NN}}$=130 GeV Au+Au collisions

K. Adcox,[40] S. S. Adler,[4] N. N. Ajitanand,[33] Y. Akiba,[14] J. Alexander,[33] L. Aphecetche,[35] Y. Arai,[14] S. H. Aronson,[4] R. Averbeck,[34] T. C. Awes,[27] K. N. Barish,[5] P. D. Barnes,[19] J. Barrette,[21] B. Bassalleck,[25] S. Bathe,[22] V. Baublis,[28] A. Bazilevsky,[12,30] S. Belikov,[12,13] F. G. Bellaiche,[27] S. T. Belyaev,[16] M. J. Bennett,[19] Y. Berdnikov,[31] S. Botelho,[32] M. L. Brooks,[19] D. S. Brown,[26] N. Bruner,[25] D. Bucher,[22] H. Buesching,[22] V. Bumazhnov,[12] G. Bunce,[4,30] J. M. Burward-Hoy,[34] S. Butsyk,[34,28] T. A. Carey,[19] P. Chand,[3] J. Chang,[5] W. C. Chang,[1] L. L. Chavez,[25] S. Chernichenko,[12] C. Y. Chi,[8] J. Chiba,[14] M. Chiu,[8] R. K. Choudhury,[3] T. Christ,[34] T. Chujo,[4,39] M. S. Chung,[15,19] P. Chung,[33] V. Cianciolo,[27] B. A. Cole,[8] D. G. d'Enterria,[35] G. David,[4] H. Delagrange,[35] A. Denisov,[12] A. Deshpande,[30] E. J. Desmond,[4] O. Dietzsch,[32] B. V. Dinesh,[3] A. Drees,[34] A. Durum,[12] D. Dutta,[3] K. Ebisu,[24] Y. V. Efremenko,[27] K. El Chenawi,[40] H. En'yo,[17,29] S. Esumi,[39] L. Ewell,[4] T. Ferdousi,[5] D. E. Fields,[25] S. L. Fokin,[16] Z. Fraenkel,[42] A. Franz,[4] A. D. Frawley,[9] S.-Y. Fung,[5] S. Garpman,[20,*] T. K. Ghosh,[40] A. Glenn,[36] A. L. Godoi,[32] Y. Goto,[30] S. V. Greene,[40] M. Grosse Perdekamp,[30] S. K. Gupta,[3] W. Guryn,[4] H.-Å. Gustafsson,[20] J. S. Haggerty,[4] H. Hamagaki,[7] A. G. Hansen,[19] H. Hara,[24] E. P. Hartouni,[18] R. Hayano,[38] N. Hayashi,[29] X. He,[10] T. K. Hemmick,[34] J. M. Heuser,[34] M. Hibino,[41] J. C. Hill,[13] D. S. Ho,[43] K. Homma,[11] B. Hong,[15] A. Hoover,[26] T. Ichihara,[29,30] K. Imai,[17,29] M. S. Ippolitov,[16] M. Ishihara,[29,30] B. V. Jacak,[34,30] W. Y. Jang,[15] J. Jia,[34] B. M. Johnson,[4] S. C. Johnson,[18,34] K. S. Joo,[23] S. Kametani,[41] J. H. Kang,[43] M. Kann,[28] S. S. Kapoor,[3] S. Kelly,[8] B. Khachaturov,[42] A. Khanzadeev,[28] J. Kikuchi,[41] D. J. Kim,[43] H. J. Kim,[43] S. Y. Kim,[43] Y. G. Kim,[43] W. W. Kinnison,[19] E. Kistenev,[4] A. Kiyomichi,[39] C. Klein-Boesing,[22] S. Klinksiek,[25] L. Kochenda,[28] V. Kochetkov,[12] D. Koehler,[25] T. Kohama,[11] D. Kotchetkov,[5] A. Kozlov,[42] P. J. Kroon,[4] K. Kurita,[29,30] M. J. Kweon,[15] Y. Kwon,[43] G. S. Kyle,[26] R. Lacey,[33] J. G. Lajoie,[13] J. Lauret,[33] A. Lebedev,[13] D. M. Lee,[19] M. J. Leitch,[19] X. H. Li,[5] Z. Li,[6,29] D. J. Lim,[43] M. X. Liu,[19] X. Liu,[6] Z. Liu,[6] C. F. Maguire,[40] J. Mahon,[4] Y. I. Makdisi,[4] V. I. Manko,[16] Y. Mao,[6,29] S. K. Mark,[21] S. Markacs,[8] G. Martinez,[35] M. D. Marx,[34] A. Masaike,[17] F. Matathias,[34] T. Matsumoto,[7,41] P. L. McGaughey,[19] E. Melnikov,[12] M. Merschmeyer,[22] F. Messer,[34] M. Messer,[4] Y. Miake,[39] T. E. Miller,[40] A. Milov,[42] S. Mioduszewski,[4,36] R. E. Mischke,[19] G. C. Mishra,[10] J. T. Mitchell,[4] A. K. Mohanty,[3] D. P. Morrison,[4] J. M. Moss,[19] F. Mühlbacher,[34] M. Muniruzzaman,[5] J. Murata,[29] S. Nagamiya,[14] Y. Nagasaka,[24] J. L. Nagle,[8] Y. Nakada,[17] B. K. Nandi,[5] J. Newby,[36] L. Nikkinen,[21] P. Nilsson,[20] S. Nishimura,[7] A. S. Nyanin,[16] J. Nystrand,[20] E. O'Brien,[4] C. A. Ogilvie,[13] H. Ohnishi,[4,11] I. D. Ojha,[2,40] M. Ono,[39] V. Onuchin,[12] A. Oskarsson,[20] L. Österman,[20] I. Otterlund,[20] K. Oyama,[7,38] L. Paffrath,[4,*] A. P. T. Palounek,[19] V. S. Pantuev,[34] V. Papavassiliou,[26] S. F. Pate,[26] T. Peitzmann,[22] A. N. Petridis,[13] C. Pinkenburg,[4,33] R. P. Pisani,[4] P. Pitukhin,[12] F. Plasil,[27] M. Pollack,[34,36] K. Pope,[36] M. L. Purschke,[4] I. Ravinovich,[42] K. F. Read,[27,36] K. Reygers,[22] V. Riabov,[28,31] Y. Riabov,[28] M. Rosati,[13] A. A. Rose,[40] S. S. Ryu,[43] N. Saito,[29,30] A. Sakaguchi,[11] T. Sakaguchi,[7,41] H. Sako,[39] T. Sakuma,[29,37] V. Samsonov,[28] T. C. Sangster,[18] R. Santo,[22] H. D. Sato,[17,29] S. Sato,[39] S. Sawada,[14] B. R. Schlei,[19] Y. Schutz,[35] V. Semenov,[12] R. Seto,[5] T. K. Shea,[4] I. Shein,[12] T.-A. Shibata,[29,37] K. Shigaki,[14] T. Shiina,[19] Y. H. Shin,[43] I. G. Sibiriak,[16] D. Silvermyr,[20] K. S. Sim,[15] J. Simon-Gillo,[19] C. P. Singh,[2] V. Singh,[2] M. Sivertz,[4] A. Soldatov,[12] R. A. Soltz,[18] S. Sorensen,[27,36] P. W. Stankus,[27] N. Starinsky,[21] P. Steinberg,[8] E. Stenlund,[20] A. Ster,[44] S. P. Stoll,[4] M. Sugioka,[29,37] T. Sugitate,[11] J. P. Sullivan,[19] Y. Sumi,[11] Z. Sun,[6] M. Suzuki,[39] E. M. Takagui,[32] A. Taketani,[29] M. Tamai,[41] K. H. Tanaka,[14] Y. Tanaka,[24] E. Taniguchi,[29,37] M. J. Tannenbaum,[4] J. Thomas,[34] J. H. Thomas,[18] T. L. Thomas,[25] W. Tian,[6,36] J. Tojo,[17,29] H. Torii,[17,29] R. S. Towell,[19] I. Tserruya,[42] H. Tsuruoka,[39] A. A. Tsvetkov,[16] S. K. Tuli,[2] H. Tydesjö,[20] N. Tyurin,[12] T. Ushiroda,[24] H. W. van Hecke,[19] C. Velissaris,[26] J. Velkovska,[34] M. Velkovsky,[34] A. A. Vinogradov,[16] M. A. Volkov,[16] A. Vorobyov,[28] E. Vznuzdaev,[28] H. Wang,[5] Y. Watanabe,[29,30] S. N. White,[4] C. Witzig,[4] F. K. Wohn,[13] C. L. Woody,[4] W. Xie,[5,42] K. Yagi,[39] S. Yokkaichi,[29] G. R. Young,[27] I. E. Yushmanov,[16] W. A. Zajc,[8,†] Z. Zhang,[34] and S. Zhou[6]

(PHENIX Collaboration)

[1]*Institute of Physics, Academia Sinica, Taipei 11529, Taiwan*

[2]*Department of Physics, Banaras Hindu University, Varanasi 221005, India*

[3]*Bhabha Atomic Research Centre, Bombay 400 085, India*

[4]*Brookhaven National Laboratory, Upton, New York 11973-5000, USA*

[5]*University of California, Riverside, California 92521, USA*

[6]*China Institute of Atomic Energy (CIAE), Beijing, People's Republic of China*

[7]*Center for Nuclear Study, Graduate School of Science, University of Tokyo, 7-3-1 Hongo, Bunkyo, Tokyo 113-0033, Japan*

[8]*Columbia University, New York, New York 10027, USA and*
Nevis Laboratories, Irvington, New York 10533, USA

[9]*Florida State University, Tallahassee, Florida 32306, USA*

[10]*McGill University, Montreal, Quebec, Canada H3A 2T8*

[11]*Hiroshima University, Kagamiyama, Higashi-Hiroshima 739-8526, Japan*

[12]*Institute for High Energy Physics (IHEP), Protvino, Russia*

[13]*Iowa State University, Ames, Iowa 50011, USA*

[14]*KEK, High Energy Accelerator Research Organization, Tsukuba-shi, Ibaraki-ken 305-0801, Japan*

[15]*Korea University, Seoul, 136-701, Korea*

[16]*Russian Research Center "Kurchatov Institute," Moscow, Russia*

[17]*Kyoto University, Kyoto 606, Japan*
[18]*Lawrence Livermore National Laboratory, Livermore, California 94550, USA*
[19]*Los Alamos National Laboratory, Los Alamos, New Mexico 87545, USA*
[20]*Department of Physics, Lund University, Box 118, SE-221 00 Lund, Sweden*
[21]*Georgia State University, Atlanta, Georgia 30303, USA*
[22]*Institut für Kernphysik, University of Muenster, D-48149 Muenster, Germany*
[23]*Myongji University, Yongin, Kyonggido 449-728, Korea*
[24]*Nagasaki Institute of Applied Science, Nagasaki-shi, Nagasaki 851-0193, Japan*
[25]*University of New Mexico, Albuquerque, New Mexico, 87131 USA*
[26]*New Mexico State University, Las Cruces, New Mexico 88003, USA*
[27]*Oak Ridge National Laboratory, Oak Ridge, Tennessee 37831, USA*
[28]*PNPI, Petersburg Nuclear Physics Institute, Gatchina, Russia*
[29]*RIKEN (The Institute of Physical and Chemical Research), Wako, Saitama 351-0198, Japan*
[30]*RIKEN BNL Research Center, Brookhaven National Laboratory, Upton, New York 11973-5000, USA*
[31]*St. Petersburg State Technical University, St. Petersburg, Russia*
[32]*Universidade de São Paulo, Instituto de Física, Caixa Postal 66318, São Paulo CEP05315-970, Brazil*
[33]*Chemistry Department, State University of New York, Stony Brook, New York 11794, USA*
[34]*Department of Physics and Astronomy, State University of New York, Stony Brook, New York 11794, USA*
[35]*SUBATECH (Ecole des Mines de Nantes, CNRS-IN2P3, Université de Nantes) Boîte Postal 20722 - 44307, Nantes, France*
[36]*University of Tennessee, Knoxville, Tennessee 37996, USA*
[37]*Department of Physics, Tokyo Institute of Technology, Tokyo, 152-8551, Japan*
[38]*University of Tokyo, Tokyo, Japan*
[39]*Institute of Physics, University of Tsukuba, Tsukuba, Ibaraki 305, Japan*
[40]*Vanderbilt University, Nashville, Tennessee 37235, USA*
[41]*Waseda University, Advanced Research Institute for Science and Engineering, 17 Kikui-cho, Shinjuku-ku, Tokyo 162-0044, Japan*
[42]*Weizmann Institute, Rehovot 76100, Israel*
[43]*Yonsei University, IPAP, Seoul 120-749, Korea*
[44]*KFKI Research Institute for Particle and Nuclear Physics (RMKI), Budapest, Hungary*
(Received 9 July 2003; published 17 February 2004)

Transverse momentum spectra and yields of hadrons are measured by the PHENIX collaboration in Au + Au collisions at $\sqrt{s_{NN}}$=130 GeV at the Relativistic Heavy Ion Collider. The time-of-flight resolution allows identification of pions to transverse momenta of 2 GeV/c and protons and antiprotons to 4 GeV/c. The yield of pions rises approximately linearly with the number of nucleons participating in the collision, while the number of kaons, protons, and antiprotons increases more rapidly. The shape of the momentum distribution changes between peripheral and central collisions. Simultaneous analysis of all the p_T spectra indicates radial collective expansion, consistent with predictions of hydrodynamic models. Hydrodynamic analysis of the spectra shows that the expansion velocity increases with collision centrality and collision energy. This expansion boosts the particle momenta, causing the yield from soft processes to exceed that for hard to large transverse momentum, perhaps as large as 3 GeV/c.

DOI: 10.1103/PhysRevC.69.024904 PACS number(s): 25.75.Dw

I. INTRODUCTION

Heavy ion reactions at ultrarelativistic energies provide information on strongly interacting matter under extreme conditions. Lattice QCD and phenomenological predictions indicate that at high enough energy density a deconfined state of quarks and gluons, the quark-gluon plasma, is formed. It is expected that conditions in ultrarelativistic heavy ion reactions may produce this new state of matter, the study of which is the major goal of the experiments at the Relativistic Heavy Ion Collider (RHIC).

The high energy density state thus created will cool down and expand, undergoing a phase transition to "ordinary" hadronic matter. While the tools of choice to study the earliest phase of the reactions, and thereby the new state, are probes that do not interact via the strong force, such as photons, electrons, or muons, the global properties and dynamics of later stages in the system are best studied via hadronic observables. Hadron momentum spectra in proton-proton reactions are often separated into two parts, a soft part at low transverse momentum p_T, where the shape is roughly exponential in transverse mass $m_T=\sqrt{p_T^2+m_0^2}$, and a high p_T region where the shape more closely resembles a power law. Soft production (low p_T) is attributed to fragmentation of a string [1,2] between components of the struck nucleons, while hard (high p_T) hadrons are expected to originate predominantly

*Deceased.
†Spokesperson. Email address: zajc@nevis.columbia.edu

from fragmentation of hard-scattered partons. The transition between these two regimes is not sharply defined, but is commonly believed to be near $p_T \approx 2$ GeV/c [3].

In proton-nucleus ($p+A$) scattering, these two regimes depend on the colliding system size in different ways. The soft production depends on the number of nucleons struck or participating in the collision ($N_{\rm part}$). The number of hard scatterings should increase proportionally to the number of binary nucleon-nucleon encounters ($N_{\rm coll}$) since these processes have a small elementary cross section and may be considered as incoherent. Hard scattering also produces color strings which fragment and produce some low-p_T particles, though these are much fewer in number than those from the much more frequent soft scatterings. In $p+A$ these $N_{\rm part}$ and $N_{\rm coll}$ are connected by a very simple relation, namely, $N_{\rm part} = N_{\rm coll} + 1$.

In nucleus-nucleus collisions, the number of participant nucleons does not scale simply with A, so it is more useful to study scaling with $N_{\rm coll}$ or $N_{\rm part}$. Collisions are sorted according to centrality, allowing control of the geometry and determination of $N_{\rm coll}$ or $N_{\rm part}$.

In heavy ion collisions, one expects secondary collisions of particles (rescattering) to take place, especially among particles with low and intermediate transverse momentum. Rescattering may occur among partons early in the collision, and also among hadrons later in the collision. Both kinds of rescattering can lead to collective behavior among the particles, and the presence of elliptic flow [4–9] indicates that partonic rescattering is important at RHIC. In the extreme, rescattering can lead to thermalization. Rescattering has observable consequences on the final hadron momentum spectra, causing them to be broadened as shown in this paper. This relates to some of the key questions regarding the evolution of the collision: Are the size and lifetime sufficient to attain local equilibrium? Are the momentum distributions thermal, and, if so, what are the chemical and kinetic freeze-out temperatures? Can expansion be described by hydrodynamic models? Momentum distributions of hadrons as a function of centrality provide a means to investigate these questions and permit extraction of thermodynamic quantities which govern the predicted phase transition.

This paper reports semi-inclusive momentum spectra and yields of π, K, and p from Au-Au collisions at $\sqrt{s_{NN}} = 130$ GeV. The data are measured and analyzed by the PHENIX Collaboration in the first year of the physics program at RHIC (Run-1).

The paper is organized as follows. In Sec. II the PHENIX detectors used in the analysis are described. The data reduction techniques using the time-of-flight and drift chamber detectors, along with the corrections applied to the spectra, are described in Sec. III. Functions that describe the shape of the spectra are used to extrapolate the unmeasured portion in order to determine the total average momentum and particle yield for each particle. The overall systematic uncertainties in the spectra are discussed. The resulting minimum bias and centrality-selected particle spectra are presented in Sec. IV. In Sec. V a description of the particle production within a hydrodynamic picture is investigated. For each centrality selection, a hydrodynamic parametrization of the m_T distribution is fit simultaneously to the spectra of different species.

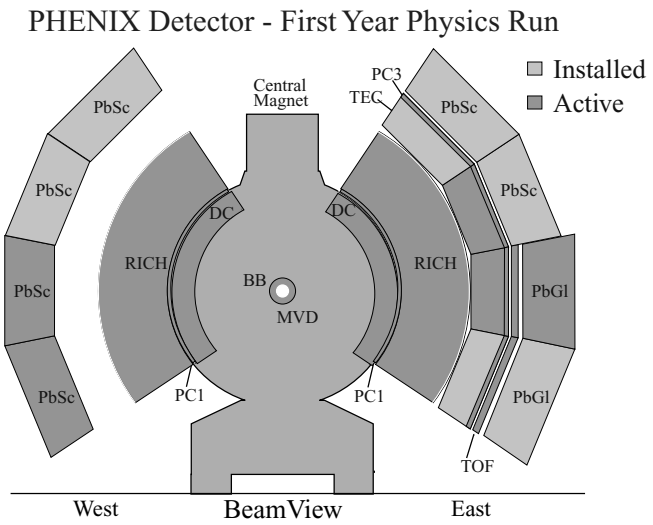

FIG. 1. A cross-sectional view of the PHENIX detector transverse to the beamline. Within the two central arm spectrometers the detectors that were instrumented and operational during the $\sqrt{s_{NN}} = 130$ GeV run are shown.

The data are compared to full hydrodynamic calculations. The transition region in p_T between hard (perturbative QCD) and soft (hydrodynamic behavior) physics is investigated by comparison of extrapolated soft spectra to the data. Finally, we study the dependence of the particle yields on the number of nucleons participating in the collision.

II. EXPERIMENT

The PHENIX [10,11] experiment at RHIC identifies hadrons over a large momentum range, by the addition of excellent time-of-flight capability to the detector suite optimized for photons, electrons, and muons. PHENIX has four spectrometer arms: two that are positioned about midrapidity (the central arms) and two at more forward rapidities (the muon arms). A cross-sectional view of the PHENIX detector, transverse to the beam line is shown in Fig. 1. Within the two central arm spectrometers, the detectors that were instrumented and operational during the $\sqrt{s_{NN}} = 130$ GeV run (Run-1) are shown. The detector systems in PHENIX are discussed in detail elsewhere [12]. The detector systems used for the measurements reported in this paper are described in detail in the following sections.

A. Central arm detectors

The central arm spectrometers use a central magnet that produces an approximately axially symmetric field that focuses charged particles into the detector acceptance. The two central arms are labeled as east and west arms. The east arm contains the following subsystems used in this analysis: drift chamber (DC), pad chamber (PC), and a time-of-flight (TOF) wall. The PHENIX hadron acceptance using the TOF system in the east arm is illustrated in Fig. 2 where the transverse momentum is plotted as a function of the particle rapidity (the phase space) within the central arm acceptance subtend-

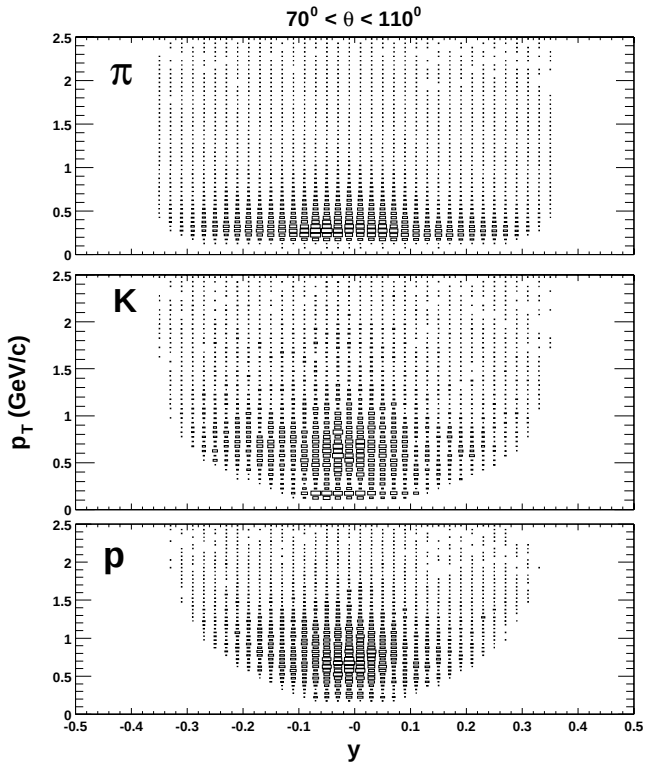

FIG. 2. The central arm spectrometer acceptance in rapidity and transverse momentum for pions (top), kaons (middle), and protons (bottom).

ing the polar angle θ from 70° to 110° for pions, kaons, and protons. The vertical lines are the equivalent pseudorapidity edges, corresponding to $|\eta|<0.35$. More details are discussed elsewhere [13].

1. Tracking chambers

The charged particle tracking chambers include three layers of pad chambers and two drift chambers. The chambers are designed to operate in a high particle multiplicity environment.

The drift chambers are the first tracking detectors that charged particles encounter as they travel from the collision vertex through the central arms. Each is 1.8 m in width in the beam direction, subtends 90° in azimuthal angle ϕ, centered at a radius $R_{\mathrm{DC}}=2.2$ m, and is filled with a 50-50 argon-ethane gas mixture. It consists of 40 planes of sense wires arranged in 80 drift cells placed cylindrically symmetric about the beam line. The wire planes are placed in an *X*-*U*-*V* configuration in the following order (moving outward radially): 12 *X* planes (*X*1)), four *U* planes (*U*1), four *V* planes (*V*1), 12 *X* planes (*X*2), four *U* planes (*U*2), and four *V* planes (*V*2). The *U* and *V* planes are tilted by a small ±5° stereo angle to allow for full three-dimensional track reconstruction. The field wire design is such that the electron drift to each sense wire is only from one side, thus removing most left-right ambiguities everywhere except within 2 mm of the sense wire. The wires are divided electrically in the middle at the beam-line center. The occupancy for a central RHIC Au+Au collision is about two hits per wire.

At the drift chamber location, the field of the central magnet is nearly zero, so the DC determines (nearly) straight-line track segments in the r-ϕ plane. Each track segment is intersected with a circle at R_{DC}, where it is characterized by two angles: the angular deflection in the main bend plane and the azimuthal position in ϕ. A combinatorial Hough transform technique is used to identify track segments by searching for location maxima in this angular space [14]. The DCs are calibrated with respect to the event collision time measurement (see Sec. II B). With this calibration, the single-wire resolution in the r-ϕ plane is 160 μm. The single-track wire efficiency is 99% and the two-track resolution is better than 1.5 mm.

The drift chambers are used to measure the momentum of charged particles and the direction vector for charged particles traversing the spectrometer. The angular deflection is inversely proportional to the component of momentum in the bend plane only. Both the bend angle and the measured track points are used in the momentum reconstruction and track model, which uses a look-up table of the measured central magnet field grid. For this dataset, the drift chamber momentum resolution is $\sigma_p/p=0.6\% \oplus 3.6\% p$, where the first term is multiple scattering up to the drift chambers and the second is the angular resolution of the detector.

In run-1, there were three pad chambers in PHENIX. Each pad chamber measures a three-dimensional space point of a charged track. The pad chambers are pixel-based detectors with effective readout sizes of 8.45 mm along the beam line by 8.40 mm in the plane transverse to the beam line. The first pad chamber layer (PC1) is fixed to the outer edge radially of each drift chamber at a radial distance of 2.49 m, while the third layer (PC3) is positioned at 4.98 m from the beam line. Both arms include PC1 chambers, while only the east arm is instrumented with PC3. The second layer (PC2) is located at an inner inscribed radius of 4.19 m in the west arm and was not installed for run-1.

The position resolution of PC1 is 1.6 mm along the beam axis and 2.3 mm in the plane transverse to the beam axis. The position resolutions of PC3 are 3.2 mm and 4.8 mm, respectively. The PC3 is used to reject background from albedo and nonvertex decay particles; however, only the PC1 is used for the results presented here. The PC1 is used in the global track reconstruction with the measured vertex position using the beam-line detectors (see Sec. II B) to determine the polar angle of each charged track. Both PC1 and the beam-line detectors provide z-coordinate information with a 1.89 mm resolution.

2. Time of flight

The TOF detector serves as the primary particle identification device for charged hadrons by the measurement of their arrival time at the TOF wall 5.1 m from the collision vertex. The TOF wall spans 30° in azimuth in the east arm. It consists of 10 panels of 96 scintillator slats each with an intrinsic timing resolution better than 100 ps. Each slat is oriented along the r-ϕ direction and provides timing as well as beam-axis position information for each particle hit recorded. The slats are viewed by two photomultiplier tubes (PMTs), attached to either end of the scintillator.

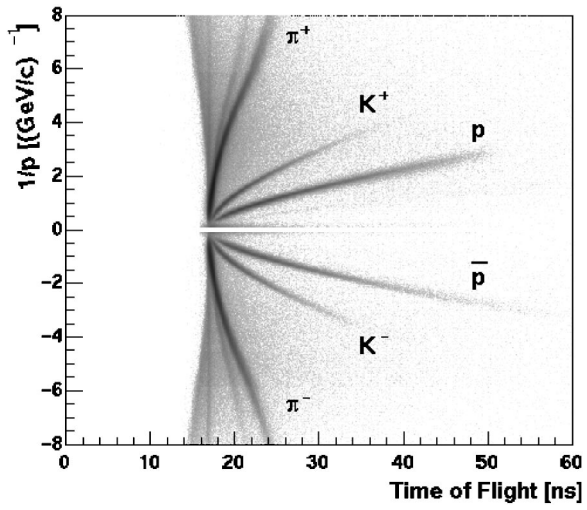

FIG. 3. Scaled time-of-flight vs reciprocal momentum in minimum-bias Au+Au collisions at $\sqrt{s_{NN}}=130$ GeV. The distribution demonstrates the particle identification capability using the TOF for the run-1 data taking period.

A $\pm 2\sigma$ π/K separation at momenta up to 2 GeV/c, and a $\pm 2\sigma$ $(\pi+K)$/proton separation up to 4 GeV/c can be achieved.

For each particle, the time, energy loss in the scintillator, and geometrical position are determined. The total time offset is calibrated slat by slat. A particle hit in the scintillator is defined by a measured pulse height which is also used to correct the time recorded at each end of the slat (slewing correction). After calibration, the average of the times at either end of the slat is the measured time for a particle. The azimuthal position is proportional to the time difference across the slat and the known velocity of light propagation in the scintillator (for Bicron BC404, this is 14 cm/ns). The slat position along the beam line determines the longitudinal coordinate position of the particle. The total time of flight is measured relative to the beam-beam counter (BBC) initial time (see Sec. II B), the measured time in the time-of-flight detector, and a global time offset from the RHIC clock. Positive pions in the momentum range $1.4<p_T<1.8$ GeV/c are used to determine the TOF resolution. The timing calibration in this analysis results in a resolution of $\sigma=115$ ps.[1]

Particle identification for charged hadrons is performed by combining the information from the tracking system with the timing information from the BBC and the TOF. Tracks at 1 GeV/c in momentum point to the TOF with a projected resolution σ_{proj} of 5 mrad in azimuthal angle and 2 cm along the beam axis. Tracks that point to the TOF with less than 2.0 σ_{proj} were selected. Figure 3 shows the resulting time of flight as a function of the reciprocal momentum in minimum-bias Au+Au collisions.

B. Beam-line detectors

The beam-line detectors determine the collision vertex position along the beam direction, and the trigger and timing information for each event. These detectors include the zero degree calorimeters (ZDCs), the BBCs, and the multiplicity vertex detector (MVD) and are positioned in PHENIX as shown in Fig. 4.

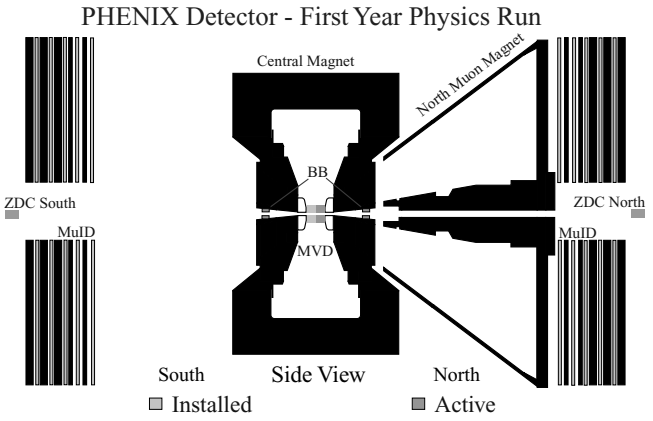

FIG. 4. A side view of the PHENIX detector parallel to the beam line. The beam line detectors determine the collision vertex position along the beam direction, and the trigger and timing information for each event.

The zero-degree calorimeters are small transverse area hadron calorimeters that are installed at each of the four RHIC experiments. They measure the fraction of the energy deposited by spectator neutrons from the collisions and serve as an event trigger for each RHIC experiment. The ZDCs measure the unbound neutrons in small forward cones ($\theta<2$ mrad) around each beam axis. Each ZDC is positioned 18 m upstream and downstream from the interaction point along the beam axis. A single ZDC consists of three modules each with a depth of two hadronic interaction lengths and read out by a single PMT. Both time and amplitude are digitized for each of the three PMTs as well as an analog sum of the PMTs for each ZDC [15].

There are two beam-beam counters each positioned 1.4 m from the interaction point, just behind the central magnet poles along the beam axis (see Fig. 4). The BBC consists of two identical sets of counters installed on both sides of the interaction point along the beam. Each counter consists of 64 Cherenkov telescopes, arranged radially about the collision axis and situated north and south of the MVD. The BBCs measure the fast secondary particles produced in each collision at forward angles, with $3.0\leqslant\eta\leqslant 3.9$, and full azimuthal coverage.

For both the ZDC and the BBC, the time and vertex position are determined using the measured time difference between the north and the south detector and the known distance between the two detectors. The start time T_0 and the vertex position along the beam axis (Z_{vertex}) are calculated as $T_0=(T_1+T_2)/2$ and $Z_{\mathrm{vertex}}=(T_1-T_2)/2c$, where T_1 and T_2 are the average timing of particles in each counter and c is the speed of light. With an intrinsic timing resolution of 150 ps, the ZDC vertex is measured to within 3 cm. In run-1, the BBC timing resolution of 70 ps results in a vertex position resolution of 1.5 cm.

Event centrality is determined using a correlation measurement between neutral energy deposited in the ZDCs and

[1]Ultimately, 96 ps results after further calibration, as reported in Ref. [12].

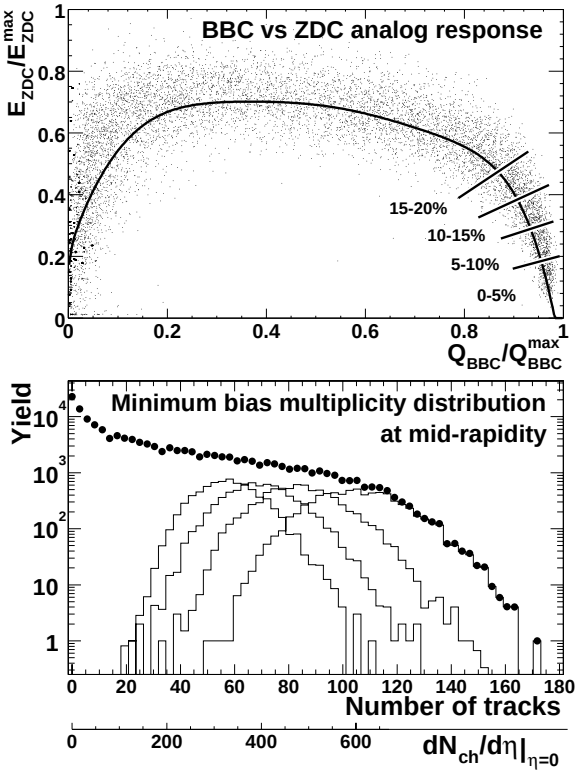

FIG. 5. The event centrality (upper plot) is determined using a correlation measurement of the fraction of neutron energy recorded in the ZDCs (vertical scale) and the fractional charge measured in the BBCs (horizontal scale). The equivalent track multiplicity in each centrality selection is shown in the lower plot.

fast particles recorded in the BBCs as shown in Fig. 5. The spectator nucleons are unaffected by the interaction and travel at their initial momentum from each respective ion. The number of neutrons measured by the ZDC is proportional to the number of spectators, while the BBC signal increases with the number of participants.

III. DATA REDUCTION AND ANALYSIS

A. Data reduction

The PHENIX Level-1 trigger selected events with hits coincident in both the ZDC and BBC detectors, and in time with the RHIC clock. A total of 5 million events were recorded at $\sqrt{s_{NN}}=130$ GeV in the ZDCs [11]. The collision position along the beam direction was required to be within ±30 cm of the center of PHENIX, using the collision vertex reconstructed by the BBC.

The trigger on both BBC and ZDC counters includes $92\pm4\%$ of the total inelastic cross section (6.8 ± 0.4 b). A Monte Carlo Glauber model [16] is used with a simulation of the BBC and ZDC responses to determine the number of nucleons participating in the collisions for the minimum-bias events. The Woods-Saxon parameters determined from electron scattering experiments are radius $R=6.38\pm0.06$ fm, diffusivity $d=0.54\pm0.01$ fm [17], and the nucleon-nucleon inelastic cross section, $\sigma^{inel}_{N+N}=40\pm3$ mb. An additional systematic uncertainty enters the radius parameter since the radial distribution of neutrons in large nuclei should be larger than for protons and is not well determined [18].

The centrality selections used in this paper are 0–5 %, 5–15 %, 15–30 %, 30–60 %, and 60–92 % of the total geometrical cross section, where 0–5 % corresponds to the most central collisions.

Only tracks that are reconstructed in all three dimensions are included in the spectra. These tracks are then matched within $2\sigma_{\rm proj}$ to the measured positions in the TOF detector. For each TOF hit, the time, position, and energy loss are measured in the TOF detector. The widths of residual distance distributions between projected tracks and TOF hit positions, $\sigma_{\rm proj}$, increase at lower momentum due to multiple scattering. Therefore, a momentum-dependent hit association criterion was defined.

Finally, a requirement on energy loss in the TOF is applied to each track to exclude false hits by requiring the energy deposit of at least minimum ionizing particle energy. A β-dependent energy loss cut whose form is a parametrization of the Bethe-Bloch formula [19] is used, where

$$dE/dx \approx \beta^{-5/3} \tag{1}$$

and $\beta=L/ct$, where L is the pathlength of the particle's trajectory from the BBC vertex to the TOF detector, t is the particle's time of flight, and c is the speed of light. The approximate Bethe-Bloch formula is scaled by a factor to fall below the data and thereby serve as a cut. The resulting equation is $\Delta E=A\beta^{-5/3}$, where A is a scaling factor equal to 1.6 MeV. The energy loss cut reduces low momentum background under the kaon and proton mass peaks. The fraction of tracks excluded after the energy loss cut is less than 5.5%.

The measured momentum p, pathlength L, and time of flight t in the spectrometer are used to calculate the particle mass, which is used for particle identification:

$$m^2 = \frac{p^2}{c^2}\left[\left(\frac{1}{\beta}\right)^2 - 1\right]. \tag{2}$$

The widths of the peaks in the mass-squared distribution depend on both momentum and time-of-flight resolutions. An analytic form for the width of m^2 as a function of momentum resolution σ_p and time-of-flight resolution is determined using Eq. (2). The error in the particle's pathlength L results in an effective time width that is included with the TOF resolution, σ_T,

$$\sigma^2_{m^2} = 4m^4\left(\frac{\sigma_p}{p}\right)^2 + 4p^4\left(\frac{\sigma_T}{\beta t}\right)^2. \tag{3}$$

The momentum resolution of the drift chambers is expressed in the following form:

$$\sigma^2_p = \left(C_1 p\frac{1}{\beta}\right)^2 + (C_2 p^2)^2, \tag{4}$$

$$C_1 = \frac{\delta\phi_{\rm ms}}{K_1}, \tag{5}$$

$$C_2 = \frac{\delta\phi_\alpha}{K_1}, \tag{6}$$

where C_1 and C_2 are the multiple scattering and angular resolution terms, respectively. The units of $\delta\phi_{\rm ms}$ are mrad GeV/c. The constant K_1 is the momentum kick on the particle from the magnetic field and is equal to 87.3 mrad GeV/c. The constant C_1 is the width in ϕ due to the multiple scattering (ms) of a charged particle with materials of the spectrometer up to the drift chambers. The C_2 term is the angular resolution of the bend angle α, which is the angular deflection in ϕ of the track segment relative to the radius to the collision vertex.

Equation (4) is used in Eq. (3) with $\beta = p/\sqrt{p^2+m^2}$, where m is the mass centroid of the particle's mass-squared distribution. The mass centroid is close to the rest mass of the particle; however due to residual misalignments and timing calibration, the centroid of the distribution is a fit parameter in order to avoid cutting into the distribution. The m^2 width for each particle is written as follows:

$$\sigma^2_{m^2} = C_1^2 4m^4\left(1+\frac{m^2}{p^2}\right) + C_2^2 4m^4p^2 + C_3^2[4p^2(m^2+p^2)], \tag{7}$$

where the coefficient C_3 is related to the combined TOF,

$$C_3 = \frac{\sigma_T c}{L}, \tag{8}$$

and pathlength contributions to the time width, σ_T in Eq. (8). From the measured drift chamber momentum resolution, $C_1 = 0.006$ and $C_2 = 0.036$ c/GeV. While the TOF resolution is 115 ± 15 ps, the pathlength uncertainty introduces a width of $\approx 20-40$ ps, so 145 ps is used for σ_T in C_3.

The pions, kaons, and protons are identified using the measured peak centroids of the m^2 distribution and selecting 2σ bands; shown as shaded regions in Fig. 6 for two different momentum slices. The 2σ bands for pions and kaons do not overlap up to $p_T = 2$ GeV/c. The protons are identified up to $p_T = 4$ GeV/c. By studying variations in the m^2 centroid and width before the particle identification cut is applied, the uncertainty in the particle identification is estimated to be 5% for all particles.

Kaons are depleted by decays in flight and geometrical acceptance. For the low momentum protons, energy loss and geometrical acceptance cause a drop in the raw yield for $p_T < 0.5$ GeV/c, as seen in Fig. 2.

The remaining background contribution was determined by reflecting the track about the midpoint of PHENIX along the beam line and repeating the association and particle identification cuts used in the TOF detector. This random background was evaluated separately for each particle type. The background contribution is $\approx 30\%$ for the kaon spectra at $0.2 < p_T < 0.4$ GeV/c and defines the low p_T limit in the spectra. The background is less than 5% in all other cases, and negligible above 0.8 GeV/c in the measured momentum range in this analysis. The background was not subtracted but is instead treated as a systematic uncertainty. This uncertainty is 2%, 5%, and 3% for pions, kaons, and protons, respectively, at $p_T < 0.6$ GeV/c and is negligible at higher momenta.

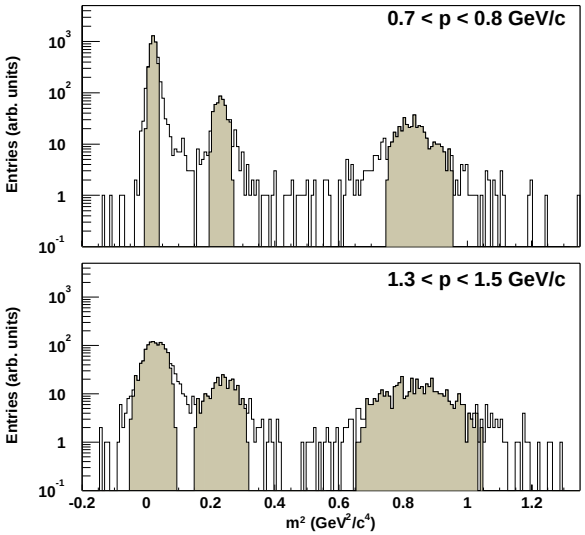

FIG. 6. (Color online) The mass-squared distributions of positive pions, kaons, and protons for two different momentum slices. The momentum slice $0.7 < p < 0.8$ GeV/c is the upper panel and $1.3 < p < 1.5$ GeV/c is the lower panel. The shaded regions correspond to the 2σ particle identification bands based on the calculated mass-squared width, the measured mass-squared centroids, and the known detector resolutions.

B. Analysis

The raw spectra include inefficiencies from detector acceptance, resolution, particle decays in flight and track reconstruction. The base-line efficiencies are determined by simulating and reconstructing single hadrons. Multiplicity dependent effects are then evaluated by embedding simulated single hadrons into real events and calculating the degradation of the reconstruction efficiency.

1. Corrections: Acceptance, decays in flight, and detector response

The corrections for the finite detector aperture, pion and kaon decays in flight, and the detector response are determined using single particles in the the GEANT [20] simulation of the detector. All details of each detector are modeled, including dead channels in the drift chambers, pad chambers, and time-of-flight detector. All physics processes are automatically taken into account, resulting in corrections for multiple scattering, antiproton annihilation, pion and kaon decays in flight, finite geometrical acceptance of the detector, and momentum resolution, which affects the spectral shape above 2.5 GeV/c.

The drift chamber simulated response is tuned to describe the response of the real drift chambers on the single-wire level. This is done using a simple geometrical model of the drift chamber and the straight-line trajectories of particles from the zero-field data. This simple model of the drift cell in the drift chamber is sufficient to describe the observed drift

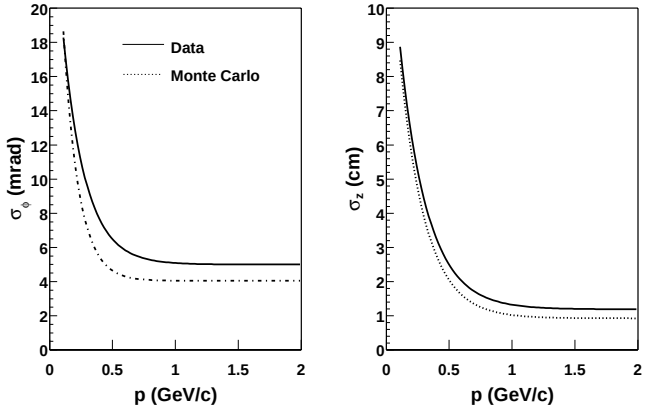

FIG. 7. Comparison of the momentum-dependent residuals of DC tracks matched to TOF hits in azimuthal angle ϕ (left) and z (right) between data (solid) and simulation (dashed).

distance distribution, the pulse width, the single-wire efficiency, and the detector resolution. The TOF response is simulated by smearing the true time of flight using a Gaussian distribution with a width as measured in the data.

Figure 7 shows the momentum dependence of the residual distance between projected tracks and TOF hits for the real (solid line) and simulated (dashed) events. These residuals are parametrized in the azimuthal angle ϕ and the beam-line direction z, separately for data and simulation. For each case, tracks that fall outside 2σ of the parametrized width are rejected, thus allowing use of the Monte Carlo to evaluate the correction for the 2σ match requirement for real tracks.

A fiducial cut is made in both the simulation and the data to ensure the same fiducial volume. The systematic uncertainty in the acceptance correction is $\approx 5\%$.

The simulated distributions are generated uniformly in p_T, ϕ, and y. For each hadron, sufficient Monte Carlo events are generated to obtain the correction factor for every measured p_T bin. The statistical errors from the correction factors were smaller than those in the data and both are added in quadrature.

The distribution of the number of particles generated in each p_T slice, dN/dp_T, is the "ideal" input distribution without detector and reconstruction effects. This distribution is normalized to 2π and 1 unit of rapidity. After detector response and track reconstruction, the output distribution is the number of particles found in each p_T slice. The final corrections are determined after an iterative weighting procedure. First, the flat input and output distributions are weighted by exponential functions for all particles using an inverse slope of 300 MeV. The ratio of input to output distributions is determined as a function of momentum. In each p_T slice, the corresponding ratio is applied to the data. The corrected data are next fitted with exponentials for kaons and protons [see Eq. (11)], and a power law for the pions [see Eq. (9)]. The original flat input and output distributions are weighted by these resulting functions. The procedure is repeated until the functions remain constant in their parameters. The weighted input and output distributions are divided to produce acceptance correction factors. The corrections are larger for kaons due to the decays in flight. The statistical error in determination of the correction factor is added in quadrature to the statistical error in the data.

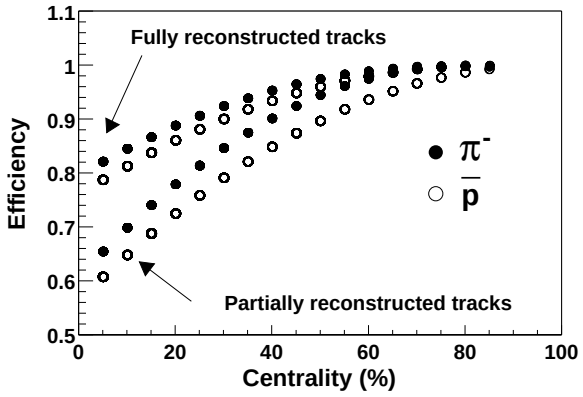

FIG. 8. The multiplicity dependent efficiency correction for pions (solid) and (anti)protons (open) for two types of tracks. The upper set of points correspond to fully reconstructed tracks in the drift chambers, while the lower set of points correspond to partially reconstructed tracks in the drift chambers.

2. High track-density efficiency correction

A final multiplicity dependent correction is determined using simulated single-particles embedded into real events. This correction depends on both the quality of the track reconstruction in a high multiplicity environment and the type of particle measured.

Depending on the centrality of the event, the correction factor is determined for each particle in the raw transverse momentum distribution and is applied as a weight. The final efficiency corrections are shown in Fig. 8, where the correction for pions is shown as solid circles and for (anti)protons as open circles. The horizontal axis ranges from the most central to the most peripheral events in increments of 5%. The systematic uncertainty in the multiplicity efficiency correction is 9%.

The difference between pions (solid) and (anti)protons (open) is due to the different TOF efficiencies for each particle (protons are slower than pions). In a small fraction of cases two particles may hit the same TOF slat at different times, and the slower particle is assigned an incorrect time. The particle will then fall outside the particle identification cuts. This effect depends on the type of particle.

For each particle, two curves are shown, representing the DC tracking inefficiency for two types of tracks: fully reconstructed and partially reconstructed tracks. Fully reconstructed tracks include $X1$ and $X2$ sections. In a high track-density environment, tracks may be partially reconstructed or hits may be incorrectly associated. There are two cases when this incorrect hit association occurs. In the first case, the direction vector in the azimuth prevents the track from pointing properly to the PC1 detector, and the correct hit cannot be associated. In the second case, the track is reconstructed properly, but there are two possible PC1 points. If no UV hits are found, then the wrong PC1 point can be associated with the track and the track's beam-line coordinate is misreconstructed. In both of these cases, the track fails the matching criteria in the TOF detector and is lost.

3. Determining the yield and mean p_T

The dN/dy and $\langle p_T \rangle$ are determined using the data in the measured region and an extrapolation to the unmeasured re-

TABLE I. The sources of systematic uncertainties in $\langle p_T \rangle$ and dN/dy.

	π(%)	K(%)	(anti)p(%)
Extrapolation	6	8	7.5
Background ($p_T < 0.6$ GeV/c)	2	5	3
$\langle p_T \rangle$ total	7	10	8
Corrections and cuts	11	11	11
dN/dy total	13	15	14

gion after integrating a functional form fit to the data. A function describing the spectral shape is fit to the data, with varying p_T ranges to control systematic uncertainties in the fit parameters. The fitted shape is extrapolated, integrated over the unmeasured range, and then combined with the measured data to get the full yield. Two different functions are used to estimate upper and lower bounds for each spectrum. The average between the upper and lower bounds is used for dN/dy and $\langle p_T \rangle$. The statistical error is determined from the data, and the systematic uncertainty is taken as half the difference between the upper and lower bounds.

For pions, a power law in p_T [Eq. (9)] and an exponential in $m_T (=\sqrt{p_T^2 + m_0^2})$ [Eq. (10)] are fit to the data. For kaons and (anti)protons, two exponentials—one in p_T [Eq. (11)] and the other in m_T—are used. The p_T exponential provides an upper limit for the extrapolated yield, which is most important for the (anti)protons. The power-law function has three parameters labeled A, p_0, and n in Eq. (9). The exponentials have two parameters, A and T.

$$\frac{d^2N}{2\pi p_T dp_T dy} = A\left(\frac{p_0}{p_0 + p_T}\right)^n, \tag{9}$$

$$\frac{d^2N}{2\pi m_T dm_T dy} = Ae^{-m_T/T}, \tag{10}$$

$$\frac{d^2N}{2\pi p_T dp_T dy} = Ae^{-p_T/T}. \tag{11}$$

C. Systematic uncertainties

In Table I, the sources of systematic uncertainties in both $\langle p_T \rangle$ and dN/dy are tabulated. The sources of uncertainty include the extrapolation in p_T, the background, and the Monte Carlo corrections, and cuts. The uncertainty in the Monte Carlo corrections is 11% and includes the multiplicity efficiency correction of 9%, the particle identification cut of 5%, and the fiducial cuts of 5%. The uncertainties in the correction functions are added in quadrature to the statistical error in the data. Background is only relevant for $p_T < 0.6$ GeV/c in the spectra.

The total systematic uncertainty in the $\langle p_T \rangle$ depends on the extrapolation and background uncertainties; the uncertainties are 7%, 10%, and 8% for pions, kaons, and protons, respectively. The overall uncertainty on dN/dy includes the uncertainties on $\langle p_T \rangle$ in addition to the uncertainties from the corrections and cuts; the uncertainties are 13%, 15%, and 14% for pions, kaons, and protons, respectively [21].

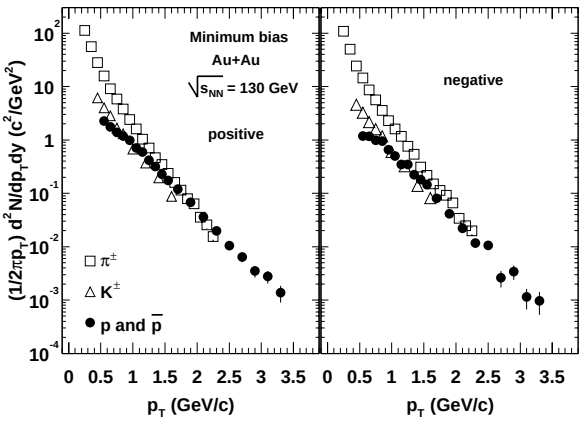

FIG. 9. The spectra of positive particles (left) and negative (right) in minimum-bias collisions from Au+Au collisions at $\sqrt{s_{NN}} = 130$ GeV. The errors include both statistical and systematic errors from the corrections.

The hadron yields and $\langle p_T \rangle$ values include an additional uncertainty arising from the fitting function used for extrapolation to the unmeasured region at low and high p_T. The magnitude of the extrapolation is $30 \pm 6\%$ of the spectrum for pions, $40 \pm 8\%$ for kaons, and $25 \pm 7.5\%$ for protons [21]. The systematic uncertainty quoted here is taken as half the difference between the results from the two different functional forms.

The momentum scale is known to better than 2%, and the momentum resolution affects the spectra shape, primarily for protons, above 2.5 GeV/c. The momentum resolution is corrected by the Monte Carlo. As other sources of uncertainty on the number of particles at any given momentum are much larger, momentum resolution effects are neglected in determining the overall systematic uncertainty from the data reduction.

IV. RESULTS

A. Transverse momentum distributions

The invariant yields as a function of p_T for identified hadrons are shown in Fig. 9, while Fig. 10 provides the centrality dependence of the spectra. The spectra are tabulated in Appendix B. The $\pi^{\pm}$, $K^{\pm}$, p, and $\bar{p}$ invariant yields for the most central, midcentral, and the most peripheral collisions, were reported previously [22]. Pion and (anti)proton invariant yields are comparable for $p_T > 1$ GeV in the most central collisions.

As can be seen already from Fig. 10 all the spectra seem to be exponential; however, upon closer inspection, small deviations from an exponential form are apparent for the more peripheral collisions. The spectrum in the most peripheral collisions is noticeably power-law-like when compared to the more exponential-like spectrum in central collisions. This is especially apparent for the pions. The effect can be seen more clearly in the ratio of the spectra for a given particle species in two different centrality classes. Such ratios

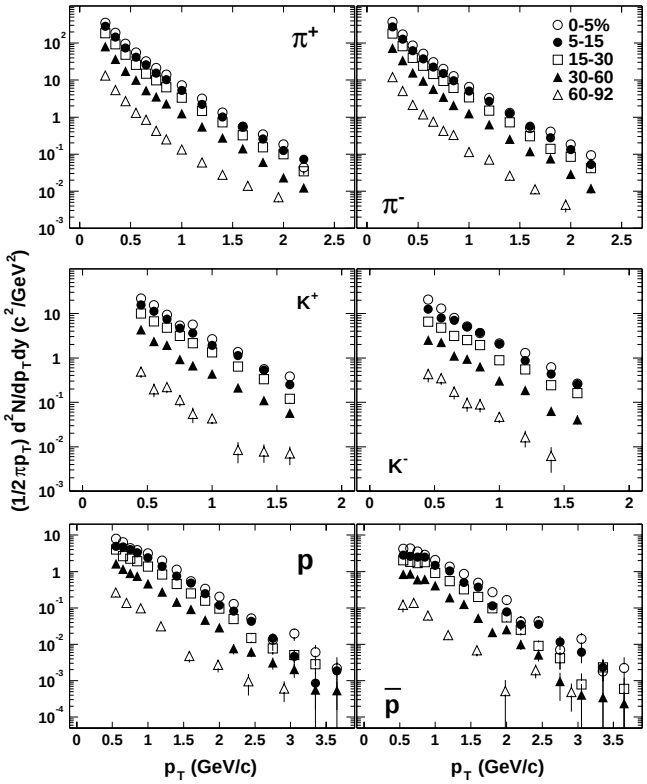

FIG. 10. The hadron spectra for five centralities from the most central 0–5 % to the most peripheral 60–92 % at $\sqrt{s_{NN}}=130$ GeV. Errors include both the statistical and point-by-point error in the corrections added in quadrature.

are shown in Fig. 11 for the 5% central and the most peripheral positive spectra (60–92 % centrality). The ratios for protons and antiprotons as well as for π^+ have a maximum at intermediate p_T and are lower at both low and high p_T. The kaon shape change is not very significant, given the current statistics.

The change in slope at low p_T in central collisions compared to peripheral is consistent with a more substantial hydrodynamic, pressure-driven transverse flow existing in central collisions, since the increased boost would tend to deplete particles at the lowest p_T (see Sec. IV C). This is observed at lower energies at the CERN SPS [23,24]. It is in contrast to results obtained at the ISR [25] for $p+p$ collisions at $\sqrt{s}=63$ GeV, where a shallow maximum or minimum exists at low p_T (in the range 0.3–0.6 GeV/c).

Feed-down contribution to p and $\bar{p}$ from inclusive Λ and $\bar{\Lambda}$

Inclusive Λ and $\bar{\Lambda}$ transverse momentum distributions have been measured in the west arm of the PHENIX spectrometer using the tracking detectors (DC, PC1) and a lead-scintillator electromagnetic calorimeter (EMCal) [26]. The invariant mass is reconstructed from the weak decays $\Lambda \rightarrow p+\pi^-$ and $\bar{\Lambda}\rightarrow \bar{p}+\pi^+$.

The tracks from the tracking detectors are required to fall within 3σ of EMCal measured space points. The EMCal timing resolution of the daughter particles is $\approx$700 ps. Using the DC momentum and the EMCal time of flight, the particle mass is calculated, and protons, antiprotons, and pions are

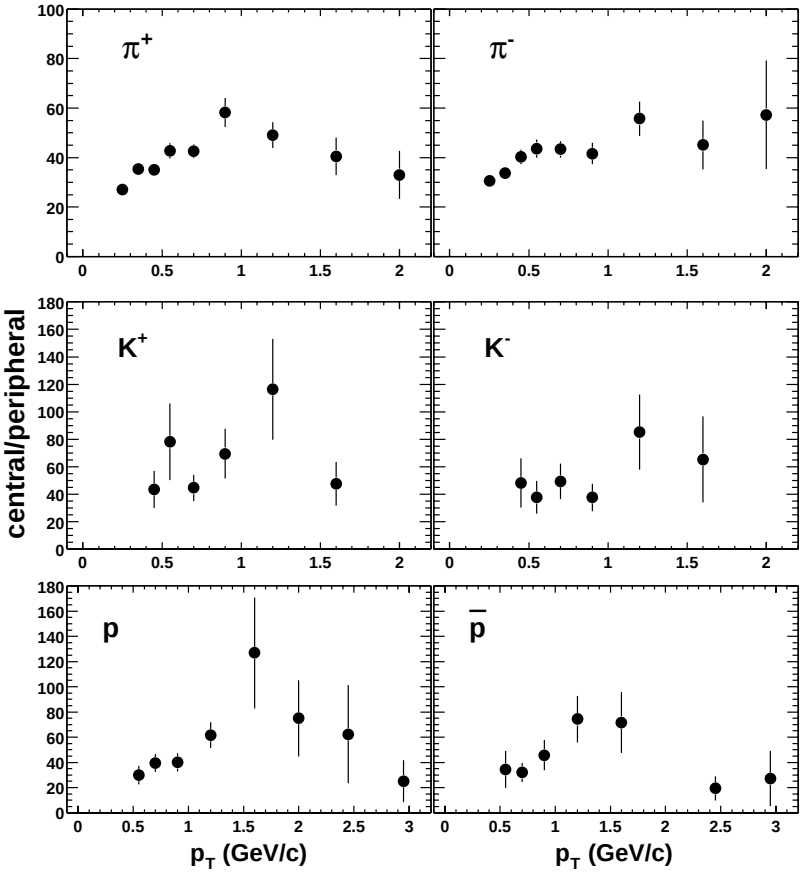

FIG. 11. The ratio of the most central to the most peripheral yields as a function of p_T for pions (top), kaons (middle), and (anti)protons (bottom).

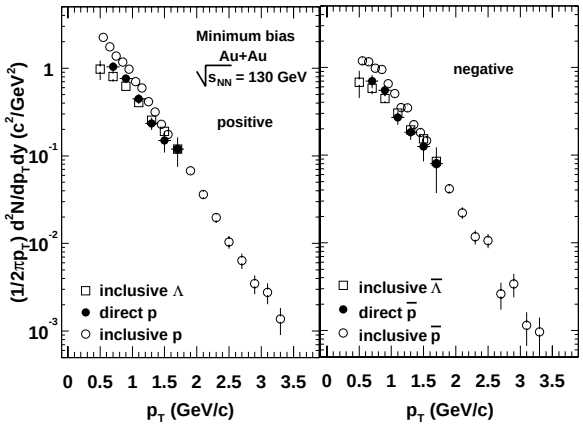

FIG. 12. For minimum-bias collisions, the inclusive Λ, inclusive p, and direct p transverse momentum distributions are plotted together in the left panel. The equivalent comparison for inclusive $\bar{\Lambda}$, $\bar{p}$, and direct $\bar{p}$ transverse momentum distributions is in the right panel.

identified using 2σ momentum-dependent mass-squared cuts. A clean particle separation is obtained using an upper momentum cut of 0.6 GeV/c and 1.4 GeV/c for pions and protons, respectively. The momentum is determined assuming the primary decay vertex is positioned at the event vertex and results in a momentum shift of 1–2% based on a Monte Carlo study.

Using all combinations of pions and protons, the invariant mass is determined. The mass distribution shows a Λ peak on top of a random combinatorial background, which is determined by combining protons and pions from different collisions with the same centrality. A signal-to-background ratio of 1/2 is obtained after applying a decay kinematic cut on the daughter particles. Fitting a Gaussian function to the mass distribution in the range $1.05 < m_{p\pi} < 1.20$ GeV/c^2, 12000 Λ and 9000 $\bar{\Lambda}$ are observed, with mass resolution $\delta m/m \approx 2\%$. The reconstructed Λ and $\bar{\Lambda}$ spectra are corrected for the acceptance, pion decay-in-flight, momentum resolution, and reconstruction efficiency [26]. The systematic uncertainty on the p_T spectra is 13% from the corrections and 3% from the combinatorial background subtraction. The feed-down contributions from heavier hyperons Σ^0 and Ω are not measured but are estimated to be $<5\%$.

Figure 12 shows the transverse momentum spectra of inclusive protons (left) and antiprotons (right) with the inclusive Λ and $\bar{\Lambda}$ transverse momentum distributions. The solid points are the (anti)proton spectra after the feed-down correction from Λ and $\bar{\Lambda}$ weak decays. From here forward, the data that are presented and discussed are not corrected for this feed-down effect; inclusive p and $\bar{p}$ yields are given. More details on the Λ and $\bar{\Lambda}$ measurement are included in Ref. [26].

TABLE III. The $\langle p_T \rangle$ in MeV/c for hadrons produced at midrapidity in each centrally class. The errors are statistical only. The systematic uncertainities are 7%, 10%, and 8% for pions, kaons, and (anti)protons, respectively.

	0–5 %	5–15 %	15–30 %	30–60 %	60–92 %
π^+	390±10	380±10	380±20	360±10	310±30
π^-	380±20	390±10	380±10	370±20	320±20
K^+	560±40	580±40	570±40	550±40	470±90
K^-	570±50	590±40	610±40	550±50	460±90
p	880±40	870±30	850±30	800±30	710±80
$\bar{p}$	900±50	890±40	840±40	820±40	800±100

B. Yield and $\langle p_T \rangle$

The yield dN/dy and the average transverse momentum $\langle p_T \rangle$ are determined for each particle as described in the preceding section and have been previously published in Ref. [22]. For each centrality, the rapidity density dN/dy and average transverse momentum $\langle p_T \rangle$ are tabulated in Tables II and III, respectively.

The $N_{\rm part}$ and $N_{\rm coll}$ in each centrality selection are determined using a Glauber-model calculation in Ref. [27]. The resulting values of $N_{\rm part}$ and $N_{\rm coll}$ are also tabulated in Table II. (See Appendix A for more detail.) The errors on $N_{\rm part}$ and $N_{\rm coll}$ include the uncertainties in the model parameters as

TABLE II. The dN/dy at midrapidity for hadrons produced at midrapidity in each centrality class. The errors are statistical only. The systematic errors are 13%, 15%, and 14% for pions, kaons, and (anti)protons, respectively. The $N_{\rm part}$ and $N_{\rm coll}$ in each centrality selection are from a Glauber-model calculation in Ref. [27], also shown with systematic errors based on a 92±4% coverage.

	0–5 %	5–15 %	15–30 %	30–60 %	60–92 %
$N_{\rm part}$	347.7±10	271.3±8.4	180.2±6.6	78.5±4.6	14.3±3.3
$N_{\rm coll}$	1008.8	712.2	405.5	131.5	14.2
π^+	276±3	216±2	141±1.5	57.0±0.6	9.6±0.2
π^-	270±3.5	200±2.2	129±1.4	53.3±0.6	8.6±0.2
K^+	46.7±1.5	35±1.3	22.2±0.8	8.3±0.3	0.97±0.11
K^-	40.5±2.3	30.4±1.4	15.5±0.7	6.2±0.3	0.98±0.1
p	28.7±0.9	21.6±0.6	13.2±0.4	5.0±0.2	0.73±0.06
$\bar{p}$	20.1±1.0	13.8±0.6	9.2±0.4	3.6±0.1	0.47±0.05

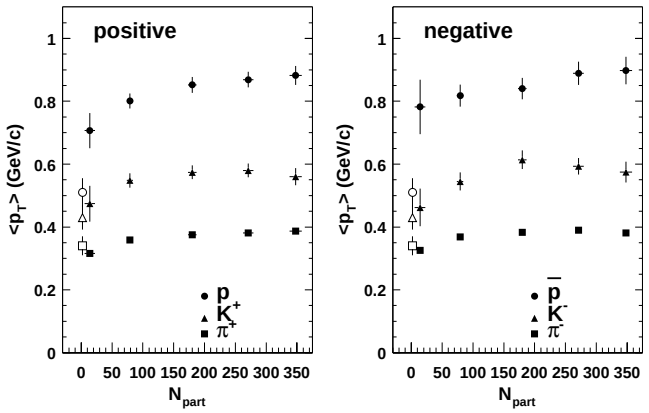

FIG. 13. The integrated mean p_T for pions, kaons, and (anti)protons produced in the five different classes of event centrality [22]. The error bars are statistical only. The systematic uncertainties are 7%, 10%, and 8% for pions, kaons, and (anti)protons, respectively. The open points are equivalent average transverse momenta from pp and $p\bar{p}$ data, interpolated to $\sqrt{s}=130$ GeV.

well as in the fraction of the total geometrical cross section $(92\% \pm 4\%)$ seen by the interaction trigger. The error due to model uncertainties is 2% [27]. An additional 3.5% error results from time dependencies in the centrality selection over the large data sample.

Pions dominate the charged particle multiplicity, but a large number of kaons and (anti)protons are produced. The inclusive yield of antiprotons is nearly comparable to that of protons. In the most central Au+Au collisions, the particle density at midrapidity (dN/dy) is ≈ 20 for antiprotons and 28 for protons, not corrected for feed-down from strange baryons.

The average transverse momenta increase with particle mass and with decreasing impact parameter. The mean transverse momentum increases with the number of participant nucleons by $20 \pm 5\%$ for pions and protons, as shown in Fig. 13. The $\langle p_T \rangle$ of particles produced in $p+p$ and $p\bar{p}$ collisions, extrapolated to RHIC energies, are consistent with the most peripheral pion and kaon data; however, the $\langle p_T \rangle$ of protons produced in Au+Au collisions is significantly higher. This dependence on the number of participant nucleons may be due to radial expansion. It should be noted that the feeding of protons and antiprotons from Λ decays affects $\langle p_T \rangle$. If the spectra are corrected for feed-down, $\langle p_T \rangle$ increases by approximately 15%.

C. Transverse mass distributions

Production of hadrons from a thermal source would make transverse mass the natural variable for analysis. Therefore we extract inverse slopes from the transverse mass distributions by separately fitting a thermal distribution to each particle species. The Boltzmann distribution is given in Eq. (12),

$$\frac{d^2N}{2\pi m_T dm_T dy} = Am_T e^{-m_T/T_{eff}}. \tag{12}$$

We use a simple exponential, however, with no powers of m_T in the prefactor, as shown in Eq. (10). This simplification is acceptable as the difference in the inverse slope is found to be less than 2%. The simple m_T exponential was also used in an equivalent analysis in Ref. [28]. The inverse slope T_{eff} can be compared to other experiments, provided the same momentum range of the spectrum is used for fitting.

If the system develops collective motion, particles experience a velocity boost from this motion, resulting in an additional transverse kinetic energy component. This motivates use of the transverse kinetic energy, i.e., transverse mass minus the particle rest mass, for plotting data. Figure 14 shows the transverse kinetic energy distributions (i.e., transverse mass minus the particle rest mass) for all positive particles (left) and negative particles (right). Pions are in the top panel, kaons in the middle panel, and (anti)protons in the bottom panel, with different symbols indicating different centrality bins. The solid lines are m_T exponential fits in the range $(m_T - m_0) < 1$ GeV for all particle species while the dashed lines are the extrapolated fits. The pion spectra follow an exponential for $0.38 < (m_T - m_0) < 1.0$ GeV while the kaons and protons appear exponential over the entire measured m_T range. The same is true for the negative particles in the right panel; however, the antiprotons have more curvature for $(m_T - m_0) < 0.5$ GeV. We extract T_{eff} by fitting exponentials of form (10) to the transverse mass spectra in the range $(m_T - m_0) < 1$ GeV.

This range is chosen common for all particle species and minimizes contributions from hard processes. Caution must be taken when comparing T_{eff} values as the local slope of the transverse mass spectra varies somewhat over m_T for pions and antiprotons even within this fit range. The resulting values of T_{eff} for all particles and centralities are tabulated in Table IV in units of MeV. The inverse slopes increase and then saturate for more central collisions for all particles except antiprotons. The fact that the inverse slope is different for mesons and baryons and for central and peripheral events is consistent with the mean p_T trends discussed above.

We compare to published inverse slopes of transverse mass distributions at midrapidity from m_T exponential fits in the region $(m_T - m_0) < 1.2$ GeV, listed in Table V. The comparison includes NA44 [28–31] and WA97 [32,33] at the SPS at $\sqrt{s_{NN}} = 17-29$ GeV; and, at $\sqrt{s_{NN}} = 23$ GeV at the ISR, Alper *et al.* [34] and Guettler *et al.* [35]. These data are chosen as they match the $m_T - m_0$ range used in fitting our data. For pions, the low-p_T region of $(m_T - m_0) < 0.3$ GeV, populated by decay of baryonic resonances, is systematically excluded from the fits. The effective temperatures are given in Table V with the references noted accordingly.

Radial flow imparts a radial velocity boost on top of the thermal distribution. Heavy particles are boosted to higher p_T, depleting the cross section at lower p_T and yielding a higher inverse slope. Therefore, the observed inverse slope dependence on both centrality and particle mass implies more radial expansion in more central collisions. At CERN SPS, the T_{eff} depends on both mass and system size (the number of participating nucleons in the collision), indicating collective expansion. The T_{eff} values at RHIC shown in Table IV are somewhat larger.

In p-p collisions at similar $\sqrt{s}$ at the ISR, hadron spectra were analyzed in transverse mass, m_T, rather than transverse

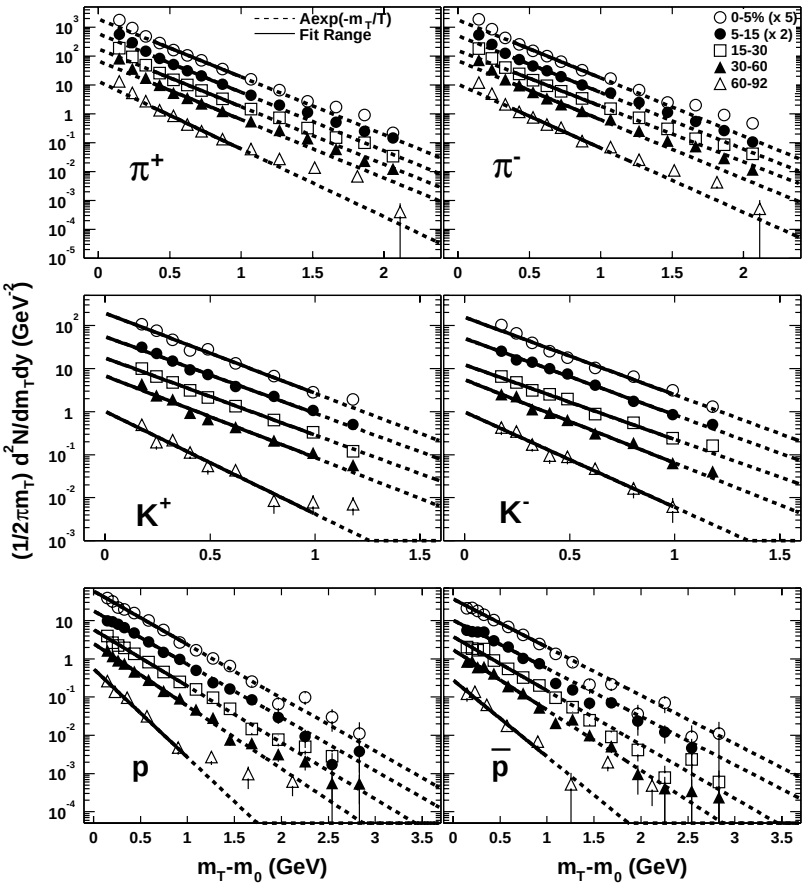

FIG. 14. Transverse mass distributions of pions (top), kaons (middle), and (anti)protons (bottom) in events with different centralities. Positive particle distributions are on the left and negative particle distributions are on the right. The solid lines are m_T exponential fits in the range $(m_T - m_0) < 1$ GeV for all particle species while the dashed lines are the extrapolated fits.

kinetic energy $m_T - m_0$ [36,37]. To facilitate a direct comparison, Fig. 15 shows the PHENIX hadron spectra, including π^0 from the 10% most central Au+Au collisions. The spectra approach one another, but do not fall upon a universal curve, and thereby fail the usual definition of scaling.

It has been suggested that at transverse mass significantly larger than the rest mass of the particle, thermal emission and radial flow may not be the only physics affecting the particle spectra. If heavy ion collisions can be described as collisions of two sheets of colored glass in which the gluon occupation number is sufficiently large to saturate, scaling of different hadron spectra with transverse mass is also predicted [38]. For Au+Au collisions at different impact parameters, the saturation scale differs, and some differences in the spectra may be expected. Nevertheless, the authors observe that the level of m_T scaling in our data is in qualitative agreement with expectations from gluon saturation [38]. Single-particle spectra alone, however, are not sufficient to disentangle saturation from flow effects.

It is often stated that m_T scaling holds in pp collisions at similar $\sqrt{s}$ to RHIC (see data, for example, in Refs. [36] and [37]). Scaling in m_T, i.e., spectra following a universal curve in m_T, might be expected if the hadrons are emitted from a source in thermal equilibrium. It is instructive to note that Ref. [36] states: "Although the curves for different particles do come together, there is no real evidence for any universal behavior in this variable." Thus, scaling at the ISR was never claimed by the original authors. In central Au+Au collisions, the slopes and yields of π, K, and p approach each other as well, but Figs. 15–17 also do not support a truly universal

TABLE IV. The resulting inverse slopes in MeV after fitting an m_T exponential to the spectra in the range $m_T - m_0 < 1$ GeV in each event centrality classes. The pion resonance is excluded in the fits. The equivalent p_T fit range for each particle is shown accordingly. The errors are statistical only.

	0–5 %	5–15 %	15–30 %	30–60 %	60–92 %
π^+ in $0.5 < p_T < 1.05$ GeV/c	216.8±5.7	214.3±4.6	217.4±4.7	214.4±5.2	176.9±9.5
π^- in $0.5 < p_T < 1.05$ GeV/c	215.8±6.5	221.2±5.6	225.3±5.8	212.8±5.7	215.8±16.8
K^+ in $0.45 < p_T < 1.35$ GeV/c	233.2±10.8	243.6±9.8	242.4±9.2	228.7±10.2	182.3±19.0
K^- in $0.45 < p_T < 1.35$ GeV/c	241.1±15.8	244.5±10.2	250.0±12.3	224.2±11.1	196.4±22.3
p in $0.55 < p_T < 1.85$ GeV/c	310.8±14.8	311.0±12.3	293.8±11.4	265.3±10.9	200.9±14.8
$\bar{p}$ in $0.55 < p_T < 1.85$ GeV/c	344.2±25.3	344.0±20.9	307.6±17.1	275.1±14.0	217.0±28.3

TABLE V. Inverse slope parameters (in MeV) of hadrons for $p+p$, $p+$nucleus, and central S+S, S+Pb, and Pb+Pb colliding at CERN energies. The errors are statistical and systematic, respectively.

Hadron	17 GeV/nucleon Pb+Pb	19.4 GeV/nucleon S+Pb	19.4 GeV/nucleon S+S	29 GeV/nucleon $p+$Pb	29 GeV/nucleon $p+$S	29 GeV/nucleon $p+$Be	23 GeV $p+p$
π^+	$156\pm6\pm23$[a]	$165\pm9\pm10$[b]	$148\pm4\pm22$[a]	$145\pm3\pm10$[b]	$139\pm3\pm10$[b]	$148\pm3\pm10$[b]	$139\pm13\pm21$[c]
K^+	$234\pm6\pm12$[a]	$181\pm8\pm10$[b]	$180\pm8\pm9$[a]	$172\pm9\pm10$[b]	$163\pm14\pm10$[b]	$154\pm8\pm10$[b]	$139\pm15\pm7$[c]
p	$289\pm7\pm14$[d]	$256\pm4\pm10$[e]	$208\pm8\pm10$[a]	$203\pm6\pm10$[e]	$175\pm30\pm10$[e]	$156\pm4\pm10$[e]	$148\pm20\pm7$[c]
Λ	$289\pm8\pm29$[f]			$203\pm9\pm20$[g]			
$\bar{\Lambda}$	$287\pm13\pm29$[f]			$180\pm15\pm18$[g]			

[a]Reference [28] (NA44 Collaboration).
[b]Reference [29] (NA44 Collaboration).
[c]References [34,35] (ISR).
[d]Reference [31] (NA44 Collaboration).
[e]Reference [30] (NA44 Collaboration).
[f]Reference [32] (WA97 Collaboration).
[g]Reference [33] (WA97 Collaboration).

behavior in m_T. Therefore the apparent puzzle of how the data could exhibit both m_T scaling and the mass-dependent p_T boost characteristic of radial flow is no puzzle at all, as any "m_T scaling" is only very approximate.

D. Summed charged particle multiplicity

As a consistency check we compare the measured rapidity densities as given in Sec. IV B to previously published pseudorapidity densities of charged particles. The measured dN/dy for each hadron species is converted to $dN/d\eta$, and the total $dN/d\eta$ is calculated by summation. Figure 18 shows $dN/d\eta$ per participant nucleon pair, compared to the measurement made by PHENIX using the pad chambers alone [27] as well as to PHOBOS and STAR yields in central collisions [40,41]. We note that the lines correspond to the fit of a linear parametrization of $N_{\rm part}$ and $N_{\rm coll}$ to the PHENIX measurement (open circles) with $a=0.88\pm0.28$ and $b=0.34\pm0.12$ as described in Ref. [42]. For the 5% central collisions, we measure 598 ± 30, and is comparable to the STAR result of 567 ± 38 [41], the PHOBOS result of 555 ± 37 [43], and the PHENIX pad chamber result of 622 ± 41 [27]. The agreement is excellent, allowing the results of this analysis to be used to decompose the particle-type dependence of the charge particle multiplicity increase with centrality.

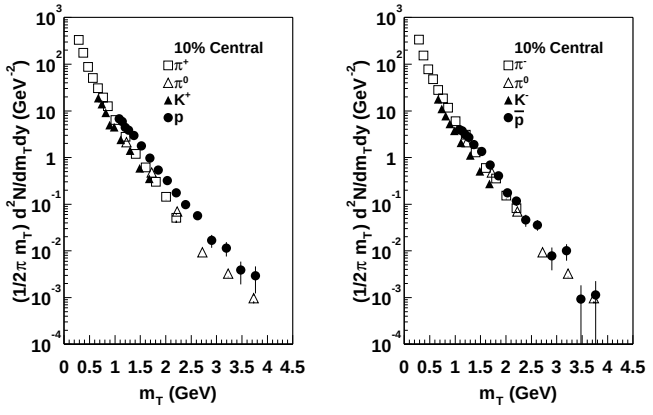

FIG. 15. The transverse mass distributions of inclusive identified hadrons produced in 10% central events, including the π^0 as measured in the electromagnetic calorimeter in PHENIX and published in Ref. [39].

V. COMPARISON WITH MODELS

A. Hydrodynamic-inspired fit

The charged particle pseudorapdity distributions are incompatible with a static thermal source, but the flat distribution observed in Ref. [43] reflects the strong longitudinal motion in the initial state. Consequently, the longitudinal momentum distribution is not an unambiguous sign of collective motion. Transverse momentum is, however, generated in the collision, so collective expansion may be more easily inferred from transverse momentum distributions.

Following the arguments of the preceding section, we analyze the particle m_T spectra. A parametrization of the m_T distribution of particles emitted from a hydrodynamic ex-

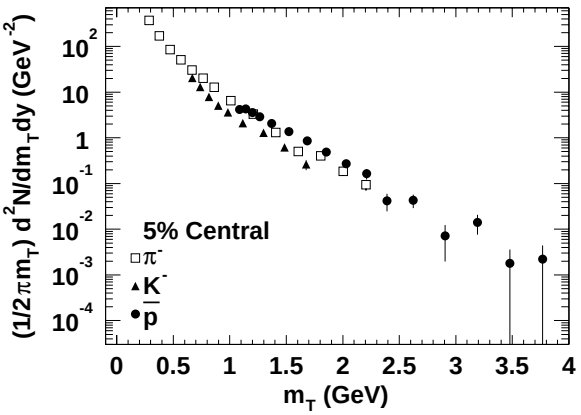

FIG. 16. The transverse mass distributions of the inclusive identified hadrons produced in the 5% central events.

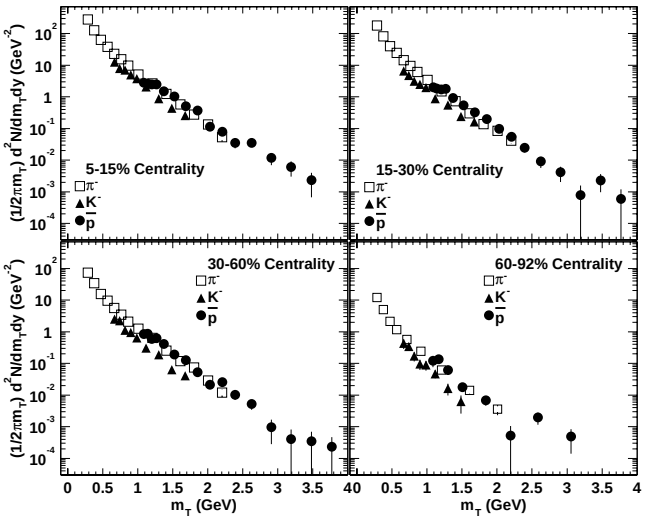

FIG. 17. The transverse mass distributions of the inclusive identified hadrons produced in events with different centralities.

panding hadron source is used. In order to determine the freeze-out temperature and collective flow without confusion from hard scattering processes, a limited p_T range is used in the fits. We include only particles with $(m_T - m_0) < 1$ GeV in the fit. Pions with $(m_T - m_0) < 0.38$ GeV are excluded to avoid resonance decays. All particles are assumed to decouple from the expanding hadron source [44] at the same freeze-out temperature $T_{\rm fo}$. This procedure allows us to extract $T_{\rm fo}$ and the magnitude of the collective boost in the transverse direction.

The inverse slope includes the local temperature of a section of the hadronic matter along with its collective velocity. The simple exponential fit of Eq. (10) treats each particle spectrum as a static thermal source, and a collective expansion velocity cannot be extracted reliably from a single-particle spectrum. However, the relative sensitivity to the

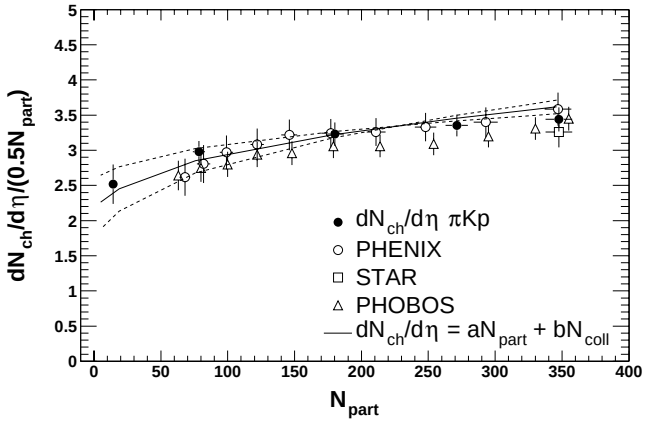

FIG. 18. Both the total charged multiplicity (open) in Refs. [40–42] and the total identified charged multiplicity (closed) scaled by the number of participant pairs are plotted together as a function of the number of participants. The lines correspond to the fit of a linear parametrization of $N_{\rm part}$ and $N_{\rm coll}$ to the PHENIX charged multiplicity measurement (open circles) with $a = 0.88 \pm 0.28$ and $b = 0.34 \pm 0.12$ as described in Ref. [42].

temperature and collective radial flow velocity differs for different particles. By using the information from all the particles, the expansion velocity can be inferred. We fit all particle species simultaneously with a functional form for a boosted thermal source based on relativistic hydrodynamics [44].

Use of this form assumes that (1) all particles decouple kinematically on a freeze-out hypersurface at the same freeze-out temperature $T_{\rm fo}$; (2) the particles collectively expand with a velocity profile increasing linearly with the radial position in the source (i.e., Hubble expansion where fluid elements do not pass through one another); and (3) the particle density distribution is independent of the radial position. Longitudinally boost-invariant expansion of the particle source is also assumed.

The transverse velocity profile is parametrized as:

$$\beta_T(\xi) = \beta_T^{\max} \xi^n, \tag{13}$$

where $\xi = r/R$, and R is the maximum radius of the expanding source at freeze-out $(0 < \xi < 1)$ [45]. The maximum surface velocity is given by $\beta_T^{\max}$, and for a linear velocity profile, $n = 1$. The average of the transverse velocity is equal to

$$\langle \beta_T \rangle = \frac{\int \beta_T^{\max} \xi^n \xi d\xi}{\int \xi d\xi} = \frac{2}{2+n} \beta_T^{\max}. \tag{14}$$

Each fluid element is locally thermalized and receives a transverse boost ρ that depends on the radial position as

$$\rho = \tanh^{-1}(\beta_T(\xi)). \tag{15}$$

The m_T dependence of the invariant yield $dN/m_T dm_T$ is determined by integrating over the rapidity, azimuthal angle, and radial distribution of fluid elements in the source. This procedure, discussed in Appendix C, yields

$$\frac{d^2N}{m_T dm_T dy} = A \int_0^1 m_T f(\xi) K_1\left(\frac{m_T \cosh(\rho)}{T_{\rm fo}}\right) I_0\left(\frac{p_T \sinh(\rho)}{T_{\rm fo}}\right) \xi d\xi. \tag{16}$$

The parameters determined by fitting Eq. (16) to the data are the freeze-out temperature $T_{\rm fo}$, the normalization A, and the maximum surface velocity $\beta_T^{\max}$ using a flat particle density distribution [i.e., $f(\xi) = 1$].

To study the parameter correlations, we make a grid of combinations of temperature and velocity, and perform a χ^2 minimization to extract the normalization A for each particle type. The fit is done simultaneously for all particles in the range $(m_T - m_0) < 1$ GeV. In addition to this upper limit in the fit, the pion fit range includes a lower limit of $(m_T - m_0) > 0.38$ GeV to avoid the resonance contribution to the low-p_T region (see Sec. V A 2).

The radial flow velocity and freeze-out temperature for all centralities are determined in the same way. The results are plotted together with the spectra in Fig. 19. The hydrody-

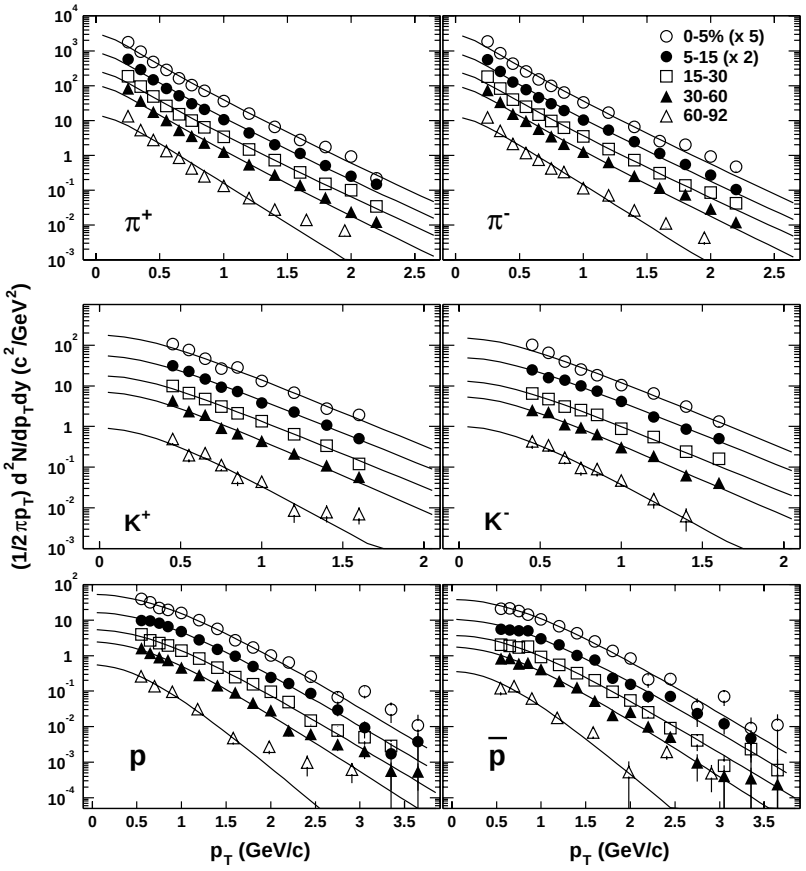

FIG. 19. The parametrization and the p_T hadron spectra for all five centrality selections.

namic form clearly describes the spectra better than the simple exponential in Fig. 14. The values for $T_{\rm fo}$ and $\beta_T^{\rm max}$ are tabulated in Table VI.

Figure 20 shows χ^2 contours for the temperature and velocity parameters for the 5% most central collisions. The n-sigma contours are labeled up to 8σ. The χ^2 contours indicate strong anticorrelation of the two parameters. If the freeze-out temperature decreases, the flow velocity increases. The minimum χ^2 is 34 and the total number of degrees of freedom (DOF) is 40. The parameters that correspond to this minimum are $T_{\rm fo}=121\pm4$ MeV and $\beta_T^{\rm max}=0.70\pm0.01$. The quoted errors are the 1σ contour widths of $\Delta\beta_T^{\rm max}$ and $\Delta T_{\rm fo}$. Within 3σ, the $T_{\rm fo}$ range is 106–141 MeV and the $\beta_T^{\rm max}$ range is 0.75–0.64.

TABLE VI. The minimum χ^2 and the parameters $T_{\rm fo}$ and $\beta_T^{\rm max}$ for each of the five centrality selections. The best fit parameters are determined by averaging all parameter pairs within the 1σ contour. The errors correspond to the standard deviation of the parameter pairs within the 1σ χ^2 contour. It is important to note that the fit range in Fig. 19 is the same as was used to fit m_T exponentials to the spectra in Fig. 14.

Centrality (%)	χ^2/DOF	$T_{\rm fo}$(MeV)	$\beta_T^{\rm max}$	$\langle\beta_T\rangle$
0–5	34.0/40	121 ± 4	0.70 ± 0.01	0.47 ± 0.01
5–15	34.7/40	125 ± 2	0.69 ± 0.01	0.46 ± 0.01
15–30	36.2/40	134 ± 2	0.65 ± 0.01	0.43 ± 0.01
30–60	68.9/40	140 ± 4	0.58 ± 0.01	0.39 ± 0.01
60–92	36.3/40	$161\pm^{19}_{12}$	$0.24\pm^{0.16}_{0.2}$	$0.16\pm^{0.16}_{0.2}$

As a linear velocity profile [$n=1$ in Eq. (13)] is assumed, the mean flow velocity in the transverse plane is $\langle\beta_T\rangle=2\beta_T^{\rm max}/3$. If a different particle density distribution [for instance, a Gaussian function for $f(\xi)$] were used, then the average should be determined after weighting accordingly [45].

A similar analysis for Pb+Pb collisions at 158A GeV, was reported by the NA49 Collaboration in Ref. [46]. Using the same hydrodynamic parametrization, simultaneous fits of several hadron species for the highest energy results in $T_{\rm fo}=127\pm1$ MeV and $\beta_T^{\rm max}=0.48\pm0.01$ with $\chi^2/NDF=120/43$ for positive particles and $T_{\rm fo}=114\pm2$ MeV and $\beta_T^{\rm max}=0.50\pm0.01$ with $\chi^2/NDF=91/41$ for negative particles (statistical errors only). Pions and deuterons are excluded from the fits to avoid dealing with resonance contributions to the pion yield and formation of deuterons by coalescence. The ϕ meson is included in the fit together with the negative particles. Previously, NA49 used a different parametrization to fit the charged hadron and deuteron spectra, as well as the m_T dependence of measured Hanbury Brown–Twiss source radii, resulting in overlapping χ^2 contours with $T_{\rm fo}=120\pm12$ MeV and $\beta_T^{\rm max}=0.55\pm0.12$ [47].

1. Velocity and particle density profile

In order to use $\beta_T^{\rm max}$ and $T_{\rm fo}$ from the fits described above, one needs to know their sensitivity to the assumed velocity and particle density profiles in the emitting source. The

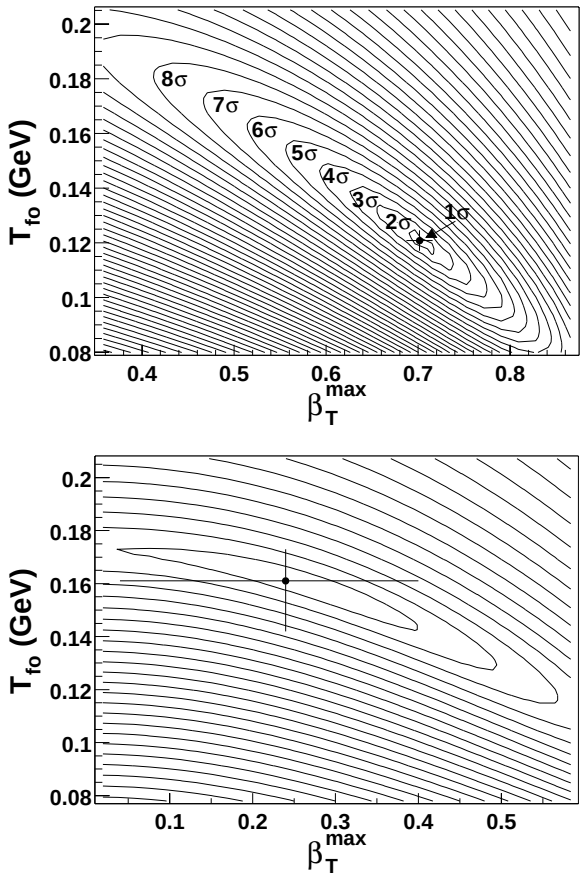

FIG. 20. The χ^2 contours in the parameter space $T_{\rm fo}$ and $\beta_T^{\rm max}$ that result after simultaneously fitting hadrons in the 0–5 % centrality (top) and 60–92 % (bottom). The n-sigma contours are labeled accordingly in the top panel. The fit results are tabulated in Table VI.

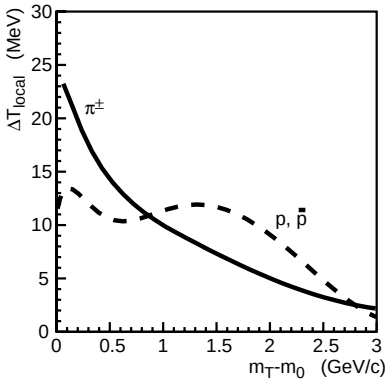

FIG. 21. The difference in the local slope for direct and inclusive pions (solid) and (anti)protons (dashed).

choice of a linear velocity profile within the source is motivated by the profile observed in a full hydrodynamic calculation [48], which shows a nearly perfect linear increase of $\beta(r)$ with r. Nevertheless, we also used a parabolic profile to check the sensitivity of the results to details of the velocity profile. For a parabolic velocity profile [$n=2$ in Eq. (13)], $\beta_T^{\rm max}$ increases by $\approx$13% and $T_{\rm fo}$ increases by $\approx$5%.

A Gaussian density profile used with a linear velocity profile increases $\beta_T^{\rm max}$ by $\approx$2%, with a negligible difference in the temperature $T_{\rm fo}$. As a test of the assumption that all the particles freeze out at a common temperature, the simultaneous fits were repeated without the kaons. The difference in $T_{\rm fo}$ is within the measured uncertainties.

2. Influence of resonance production

The functional forms given by Eqs. (10) and (17) do not include particles arising from resonance or weak decays. As resonance decays are known to result in pions at low transverse momenta [49–51], we place a p_T threshold of 500 MeV/c on pions included in the hydrodynamic fit. A similar approach was followed by NA44, E814, and other experiments at lower energies, which performed in-depth studies of resonance decays feeding hadron spectra. However, these were for systems with higher baryon density, so we performed a cross-check on possible systematic uncertainties arising from the pion threshold used in the fits. To estimate the effect of resonance decays were they not excluded from the fit, we calculate resonance contributions following Wiedemann [52].

In order to reproduce the relative yields of different particle types, a chemical freeze-out temperature—different from the kinetic freeze-out temperature—and a baryonic chemical potential are introduced. Direct production and resonance contribution are calculated for pions and (anti)protons assuming a kinetic freeze-out temperature of 123 MeV, a transverse flow velocity of 0.612 (equivalent to $\langle\beta_T\rangle = 0.44$), a baryon chemical potential of 37 MeV, and a chemical freeze-out temperature (when particle production stops) of 172 MeV. These parameters are chosen as they provide a reasonable description of the (anti)proton and pion spectra and yields (10% most central) and are in good agreement with chemical freeze-out analyses [53]. Most spectra from resonance decays show a steeper falloff than the direct production, which should lead to a smaller apparent inverse slope, depending on what fraction of the low p_T part of the spectrum is included in the fits.

To measure the effect of resonance production on the spectral shape, the local slope is determined. For a given m_T bin number i, the local slope is defined as

$$T_{\rm local}(i) = -\frac{m_T(i+1) - m_T(i-1)}{\ln[N(i+1)] - \ln[N(i-1)]}, \qquad (17)$$

which is identical to the inverse slope independent of m_T for an exponential.

The difference in the local slope,

$$\Delta T_{\rm local} = T_{\rm local}^{\rm direct} - T_{\rm local}^{\rm incl}, \qquad (18)$$

is determined for direct and inclusive pions and (anti)protons. The differences are plotted as a function of $m_T - m_0$ in Fig. 21. The difference in the local slope for protons is below 13 MeV for the full transverse mass range; the nonmonotonic behavior for protons is caused by the relatively strong transverse flow. For pions, $\Delta T_{\rm local}$ decreases monotonically with m_T and is below 10 MeV above m_T

$=1$ GeV/c. A fit of an exponential to the pion spectra for $(m_T - m_0) > 0.38$ GeV (which corresponds to $p_T > 0.5$ GeV/c) yields a difference in the inverse slope of 16 MeV with and without resonances.

B. Comparison with hydrodynamic models

Hydrodynamic parametrizations as used in the preceding Section rely upon many simplifying assumptions. Another approach to the study of collective flow is to compare the data to hydrodynamic models. Such models assume rapid equilibration in the collision and describe the subsequent motion of the matter using the laws of hydrodynamics. Large pressure buildup is found, and we investigate this ansatz by checking the consistency of the data with calculations using a reasonable set of initial conditions. We compare to two separate models, the hydrodynamics model of Kolb and Heinz [54–56] and the "hydro to hadrons" (H2H) model of Teaney and Shuryak [57,58]. The H2H model consists of a hydrodynamics calculation, followed by a hadronic cascade after chemical freeze-out. The cascade step utilizes the relativistic quantum molecular dynamics (RQMD) model, developed for lower energy heavy ion collisions [59].

In both models, initial conditions are tuned to reproduce the shape of the transverse momentum spectra measured in the most central collisions, along with the charged particle yield. Each model also includes the formation and decay of resonances.

In the Kolb and Heinz model [54–56], the initial parameters are the entropy density, baryon number density, the equilibrium time, and the freeze-out temperature which controls the duration of the expansion. The chemical freeze-out temperature is the temperature at which particle production ceases. The initial entropy or energy density and maximum temperature are fixed to match the measured multiplicity for the most central collisions using a parametrization that is tuned to produce the measured $dN_{\rm ch}/d\eta$ dependence on both $N_{\rm part}$ and $N_{\rm coll}$. A kinetic freeze-out temperature of $T_{\rm fo} = 128$ MeV is used. Spectra from the Kolb-Heinz hydrodynamic model are shown in Fig. 22 for pions (upper) and for protons (lower) as dotted lines. The solid lines are the results from the fits described in the previous sections. Figure 22 thus allows two comparisons. The similarity of the dashed and solid lines shows that the hydrodynamic-inspired parametrization used to fit the data results in a p_T distribution similar to this hydrodynamic calculation. Comparing the dashed lines to the data points shows that the hydrodynamic model agrees quite well for most of the centrality ranges. It is important to note that the model parameters are uncertain at the level of 10%, and, more importantly, the application of hydrodynamics to peripheral collisions may be less reasonable than for central collisions, as hydrodynamic calculations assume strong rescattering and a sufficiently large system size (discussed in Ref. [56]).

In Refs. [57,60], the PHENIX $\bar{p}$ spectrum shape is well described by the H2H model with the LH8 equation of state. The cascade step in the H2H model removes the requirement that all particles freeze out at a common temperature. Thus the freeze-out temperature and its profile are predicted, rather

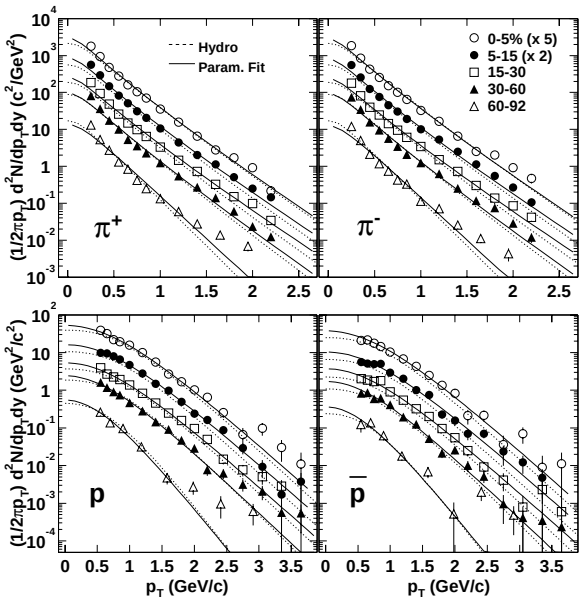

FIG. 22. The hydrodynamics calculation with initial parameters tuned to match the most central spectra in the p_T range 0.3–2.0 GeV/c.

than input parameters. Furthermore, following the hadronic interactions explicitly with RQMD removes the need to rescale the particle ratios at the end of the calculation, as they are fixed by the hadronic cross sections rather than at some particular freeze-out temperature. The LH8 equation of state includes a phase transition with a latent heat of 0.8 GeV. In Refs. [57,60], the Ω and the ϕ are shown to decouple from the expanding system at $T = 160$ MeV, and they receive a flow velocity boost of $0.45c$. Pions and kaons decouple at $T = 135$ MeV with flow velocity equal to 0.55c, while protons have $T = 120$ MeV and flow velocity greater than or equal to 0.6. These temperatures and flow velocities are consistent with the values extracted from the data for the most central events. However, the average initial energy density exceeds the experimental estimate using formation time $\tau_0 = 1$ fm/c.

Figure 23 shows radial flow from the fits of the preceding section as a function of the number of participants for $T_{\rm fo}$ (top) and $\langle \beta_T \rangle$ (bottom). There is a slight decrease of $T_{\rm fo}$, while $\langle \beta_T \rangle$ increases with $N_{\rm part}$, saturating at 0.45. The value of $\langle \beta_T \rangle$ from Kolb and Heinz [54–56] is also shown, and agrees with the data reasonably well. In the plot of $\langle \beta_T \rangle$, the dashed line indicates the results of fitting the parametrization to the data while keeping $T_{\rm fo}$ fixed at 128 MeV to agree with the value used by Kolb and Heinz. Radial flow values for central collisions remain unchanged, while those in peripheral collisions increase. Even with the extreme assumption that all collisions freeze out at the same temperature, regardless of centrality, the trend in the centrality dependence of the radial flow does not change. $\langle \beta_T \rangle$ would increase somewhat if a full feed-down correction for protons and antiprotons could be made. The low-p_T part of the spectrum would flatten slightly, as seen in Fig. 12. The resulting hydrodynamic-inspired fit to the data, shown as the solid line in Fig. 22, would be drawn nearer to the Kolb-Heinz hydrodynamic model indicated by the dashed lines in Fig. 22.

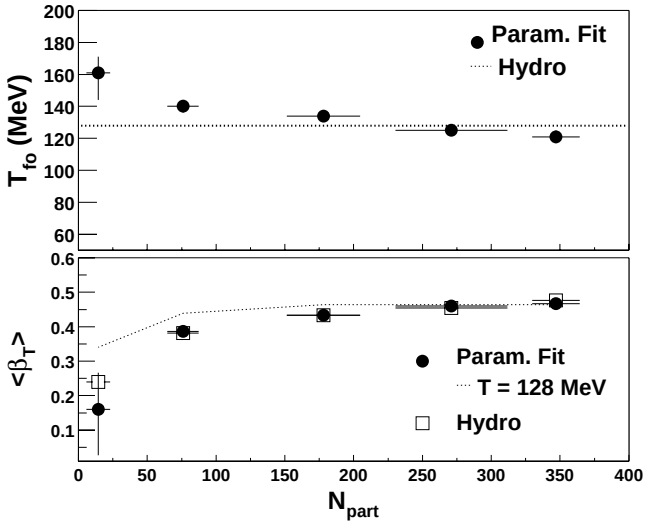

FIG. 23. The expansion parameters $T_{\rm fo}$ and $\beta_T^{\rm max}$ as a function of the number of participants. As a comparison, the results from a hydrodynamic model calculation are also shown (Refs. [54–56]). The dashed line corresponds to a fixed temperature of 128 MeV for all centralities in the parametrized fit to the data.

C. Hydrodynamic contributions at higher p_T

We use the parameters extracted from the fit to the charged hadron spectra in the low-p_T region to extrapolate the effect of the soft physics to higher p_T. This yields a prediction for the spectra of hadrons should a collective expanding thermal source be the only mechanism for particle production in heavy ion collisions. Comparing this prediction to the measured spectrum of charged particles or neutral pions should indicate the p_T range over which soft thermal processes dominate the cross section. Where the data deviate from the hydrodynamic extrapolation, other contributions, as, e.g., from hard processes or nonequilibrium production become visible. The approach described here differs from hydrodynamic fits to the entire hadron spectrum, as we fix the parameters from the low-p_T region alone, where soft physics should be dominant.

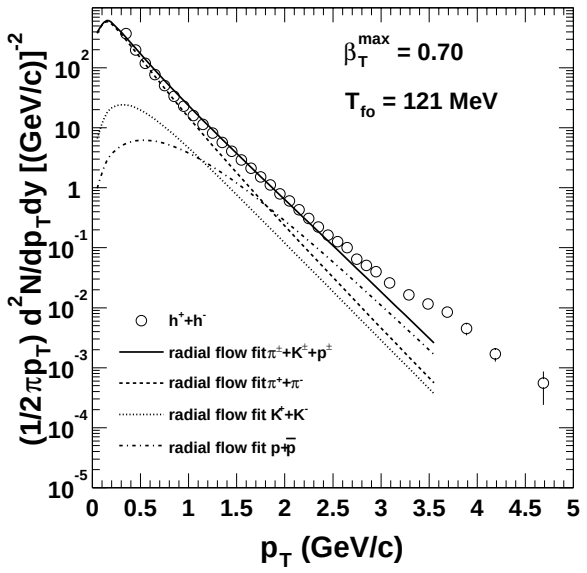

FIG. 24. The high-p_T hadron spectra in Ref. [39] compared to the fit results assuming radial flow from the π, K, p spectra in the 5% central events.

TABLE VII. Fit parameters for each particle species using Eqs. (19) and (20).

Particle	$\alpha_{\rm part}$	$\alpha_{\rm coll}$
π^+	1.06±0.01	0.79±0.01
π^-	1.08±0.01	0.80±0.01
K^+	1.18±0.02	0.88±0.02
K^-	1.20±0.03	0.89±0.02
p^+	1.16±0.02	0.86±0.02
p^-	1.14±0.03	0.84±0.02

The hadron spectrum is calculated using the fit parameters from the low-p_T region fits shown in the preceding section, and extrapolated to higher p_T. Figure 24 shows the calculated spectrum for each particle type, and the sum of the extrapolated spectra is compared to the measured charged hadrons $(h^+ + h^-)$ in the 5% most central collisions. As nonidentified charged hadrons are measured in η rather than in y, the extrapolated spectra are converted to units of η. This conversion is most important in the low-p_T region. No additional scale factor is applied—the extrapolation and data are compared absolutely. Below $\approx$2.5 GeV/c p_T, the agreement is very good, while at higher p_T the data begin to exceed the hydrodynamic extrapolation.

Other hydrodynamic calculations have been successful in describing the distributions over the full p_T range [61] with different parameter values. There are clear indications that particle production from a hydrodynamic source, if invoked to explain the spectra at low p_T, will have a non-negligible influence even at relatively large p_T. Furthermore, the range of p_T populated by hydrodynamically boosted hadrons is species dependent. This is clearly visible in Fig. 24, which shows that the extrapolated proton spectra have a flatter p_T distribution than the extrapolated pions and kaons. The yield of the "soft" protons reaches, and even exceeds, that of the extrapolated soft pions at 2.5 GeV/c p_T. Therefore the transition from soft to hard processes must also be species dependent, and the boost of the protons causes the region

TABLE VIII. Values of the parameters n_{pp} and x from fitting Eq. (21) to the observed dN/dy per $N_{\rm part}$.

	n_{pp}	x
π^+	1.41±0.11	0.028±0.020
π^-	1.10±0.11	0.085±0.030
K^+	0.130±0.021	0.232±0.076
K^-	0.089±0.020	0.326±0.132
p	0.089±0.013	0.181±0.062
$\bar{p}$	0.062±0.010	0.172±0.068

where hard processes dominate the inclusive charged particle spectrum to be at significantly higher transverse momenta in central Au+Au than in $p+p$ collisions. Our analysis suggests this occurs not lower than $p_T=3$ GeV/c.

D. Hadron yields as a function of centrality

The preceding discussion focused on the hadron spectra; now we turn to the centrality dependence of the pion, kaon, proton, and antiproton yields, which can shed further light on the importance of different mechanisms in particle production. It is instructive to see whether yields of the different hadrons scale with the number of participant nucleons, $N_{\rm part}$, the number of binary nucleon-nucleon collisions, $N_{\rm coll}$, or some combination of the two.

The total yields of the hadrons may be expected to be dominated by soft processes, and the wounded nucleon model of soft interactions suggests that the yields should scale as the number of participants, $N_{\rm part}$. If each participant loses a certain fraction of its incoming energy, as, e.g., in string models, where each pair of participants (or wounded nucleons) contributes a color flux tube, the total energy of the fireball formed at central rapidity would be proportional to the number $N_{\rm part}$ of participants. If, furthermore, the fireball is locally thermalized and particle production is determined at a single temperature, the multiplicity would scale with $N_{\rm part}$. On the other hand, at very high p_T, particle production may be dominated by hard processes and scale with $N_{\rm coll}$ [62,63].

In order to investigate the existence of scaling, the multiplicities are parametrized as

$$\frac{dN}{dy} = C(N_{\rm part})^{\alpha_{\rm part}} \tag{19}$$

and

$$\frac{dN}{dy} = C'(N_{\rm coll})^{\alpha_{\rm coll}}. \tag{20}$$

Fit results for these parametrizations are shown in Table VII. As can be seen, the exponents $\alpha_{\rm part}$ are >1 for all species, while $\alpha_{\rm coll}$ is consistently <1. The production of all particles increases more strongly than with $N_{\rm part}$, but not as strongly as with $N_{\rm coll}$. Small differences between the different particle species are apparent: The (anti)proton yield increases more strongly than the pion yield, and the kaon

TABLE IX. Invariant yields for $\pi^{\pm}$, $K^{\pm}$, and (anti)p measured in minimum-bias events at midrapidity and normalized to one rapidity unit. The errors are statistical only.

p_T(GeV/c)	$\pi^{\pm}$	$K^{\pm}$	$p(\overline{p})$
0.25	112±2		
	109±2		
0.35	56±1		
	49.9±0.9		
0.45	28.0±0.5	6.1±0.4	
	24.1±0.5	4.6±0.4	
0.55	15.7±0.3	4.0±0.3	2.3±0.1
	14.6±0.3	3.2±0.2	1.2±0.1
0.65	9.1±0.2	2.8±0.2	1.8±0.1
	8.7±0.2	2.1±0.2	1.17±0.09
0.75	5.8±0.1	1.7±0.1	1.38±0.08
	5.6±0.2	1.6±0.1	0.98±0.07
0.85	3.8±0.1	1.30±0.08	1.18±0.07
	3.6±0.1	1.17±0.09	0.95±0.07
0.95	2.40±0.08	0.87±0.06	0.98±0.06
	2.28±0.08	0.69±0.06	0.65±0.05
1.05	1.61±0.06	0.62±0.04	0.70±0.04
	1.61±0.06	0.53±0.05	0.50±0.04
1.15	103±0.04	0.43±0.03	0.60±0.04
	1.17±0.05	0.38±0.04	0.35±0.03
1.25	0.71±0.03	0.33±0.03	0.41±0.03
	0.76±0.04	0.27±0.03	0.34±0.03
1.35	0.46±0.02	0.20±0.02	0.32±0.02
	0.54±0.03	0.16±0.02	0.22±0.02
1.45	0.35±0.02	0.17±0.02	0.23±0.02
	0.31±0.02	0.13±0.02	0.18±0.02
1.55	0.24±0.02	0.10±0.01	0.17±0.02
	0.22±0.02	0.10±0.01	0.15±0.02
1.65	0.16±0.01	0.08±0.01	
	0.15±0.01	0.07±0.01	
1.70			0.119±0.008
			0.080±0.007
1.75	0.11±0.01		
	0.11±0.01		
1.85	0.079±0.008		
	0.092±0.009		
1.90			0.068±0.006
			0.041±0.005
1.95	0.063±0.007		
	0.066±0.008		
2.05	0.036±0.005		
	0.034±0.005		
2.10			0.036±0.004
			0.022±0.003
2.15	0.026±0.004		
	0.025±0.004		
2.25	0.015±0.003		

TABLE X. Pion inavariant yields in each event centrally and p_T bin measured at midrapidity, normalized to one rapidity unit. For each measured p_T bin, the postitive pion yield is the top row and the negative pion yield is the bottom row. Errors are statistical only.

p_T(GeV/c)	0–5 %	5–15 %	15–30 %	30–60 %	60–92 %
0.25	355±9	282±6	186±4	81±2	13.2±0.5
	371±10	275±7	180±4	74±2	12.1±0.5
0.35	188±5	146±3	93±2	36.6±0.8	5.3±0.2
	169±5	128±3	82±2	34.3±0.9	5.0±0.2
0.45	95±3	74±2	48±1	17.5±0.5	2.7±0.1
	86±3	63±2	40±1	15.7±0.5	2.1±0.1
0.55	56±2	41±1	26.0±0.7	10.1±0.3	1.32±0.09
	51±2	38±1	24.5±0.8	9.6±0.3	1.18±0.09
0.65	32±1	25.6±0.8	15.0±0.5	5.3±0.2	
	30±1	22.6±0.8	14.5±0.5	5.7±0.2	
0.70					0.62±0.04
					0.57±0.04
0.75	21.1±0.9	15.4±0.6	9.9±0.4	3.6±0.1	
	20±1	15.3±0.6	9.5±0.4	3.5±0.2	
0.85	14.0±0.7	10.3±0.4	6.4±0.3	2.3±0.1	
	12.8±0.8	9.6±0.5	6.1±0.3	2.1±0.1	
0.90					0.19±0.02
					0.24±0.02
1.00	7.1±0.3	5.3±0.2	3.4±0.1	1.25±0.05	
	6.5±0.3	5.0±0.2	3.4±0.1	1.25±0.05	
1.20	3.2±0.2	2.2±0.1	1.47±0.07	0.55±0.03	0.064±0.006
	3.3±0.2	2.6±0.1	1.51±0.08	0.63±0.04	0.061±0.007
1.40	1.3±0.1	1.01±0.07	0.72±0.04	0.27±0.02	
	1.3±0.1	1.25±0.09	0.72±0.05	0.26±0.02	
1.60	0.55±0.07	0.57±0.05	0.33±0.03	0.14±0.01	0.015±0.003
	0.51±0.07	0.57±0.05	0.30±0.03	0.12±0.01	0.014±0.003
1.80	0.35±0.05	0.25±0.03	0.15±0.02	0.060±0.008	
	0.40±0.06	0.27±0.03	0.14±0.02	0.075±0.009	
2.00	0.18±0.03	0.13±0.02	0.10±0.01	0.023±0.004	0.005±0.001
	0.18±0.04	0.13±0.02	0.09±0.01	0.029±0.005	0.004±0.001
2.20	0.043±0.02	0.07±0.01	0.034±0.007	0.012±0.003	
	0.09±0.03	0.05±0.01	0.042±0.009	0.012±0.003	

yield shows the strongest centrality dependence. Remarkably, the yield fraction scaling beyond linear with N_{part} is larger for kaons, protons, and antiprotons than for pions. Perhaps it is not surprising that the yields do not scale simply with N_{part}; the collective flow seen in the p_T spectra already shows that the nucleon-nucleon collisions cannot be independent.

It should be noted that scaling with multiplicity is not actually a good expectation for kaons. Kaon production at the CERN SPS can be well understood with a statistical hadronization model [64,65], if one takes into account the fact that strangeness must be produced in the collisions in $s\bar{s}$ pairs. Strangeness production is suppressed in pp collisions by phase space limitations for $s\bar{s}$ pair production. This suppression, well described by a canonical ensemble treatment, gradually fades away with increasing reaction volume, and grand canonical descriptions suffice for central Au+Au collisions [66]. Therefore, simple scaling with N_{part} should not be expected for kaons. This does not, of course, explain the rise of baryon and antibaryon production faster than linear with N_{part}.

We next check whether the simple model of hadron yields can be brought into agreement with the data by adding a component of the yields scaling as the number of binary collisions, N_{coll}. Such an admixture inspires simple two-component models [62,63]. The nonlinearity of dN/dy on the number of participants is illustrated by the ratio $(dN/dy)/N_{\mathrm{part}}$, shown in Fig. 25 as a function of centrality. The yields are seen to depend linearly on $N_{\mathrm{coll}}/N_{\mathrm{part}}$. As seen already from the exponents in Table VII, the increase with

TABLE XI. Kaon invariant yields in each event centrality and p_T bin, measured at midrapidity and normalized to one rapidity unit. The top row in each p_T bin is K^+, and the bottom row is K^-. Errors are statistical only.

p_T(GeV/c)	0–5 %	5–15 %	15–30 %	30–60 %	60–92 %
0.44					0.5±0.1
					0.4±0.1
0.45	21±3	16±2	10±1	4.3±0.5	
	21±3	13±2	7±1	2.5±0.4	
0.54					0.20±0.07
					0.3±0.1
0.55	15±2	11±1	6.6±0.7	2.4±0.3	
	13±2	8±1	4.8±0.6	2.3±0.3	
0.65	9±1	7.5±0.7	4.7±0.4	1.9±0.2	
	8±1	7.0±0.8	3.1±0.4	1.1±0.2	
0.69					0.18±0.03
					0.14±0.03
0.75	5.3±0.7	4.6±0.5	3.1±0.3	0.9±0.1	
	5.1±0.8	5.0±0.6	2.5±0.3	0.9±0.1	
0.85	5.7±0.7	3.6±0.4	2.1±0.2	0.67±0.08	
	3.6±0.6	3.7±0.4	2.0±0.2	0.64±0.09	
0.89					0.07±0.02
					0.09±0.02
0.95	3.0±0.4	2.3±0.2	1.5±0.2	0.51±0.07	
	2.4±0.4	2.3±0.3	1.0±0.2	0.35±0.06	
1.05	2.3±0.3	1.5±0.2	1.2±0.1	0.37±0.05	
	1.8±0.3	1.8±0.2	0.8±0.1	0.27±0.05	
1.15	1.6±0.3	1.3±0.2	0.62±0.09	0.29±0.04	
	1.4±0.3	0.9±0.2	0.7±0.1	0.23±0.04	
1.17					0.012±0.004
					0.015±0.005
1.25	1.1±0.2	1.0±0.1	0.66±0.09	0.15±0.03	
	1.2±0.2	0.8±0.1	0.41±0.08	0.15±0.03	
1.35	0.6±0.1	0.6±0.1	0.35±0.05	0.12±0.02	
	0.9±0.2	0.5±0.1	0.22±0.05	0.05±0.02	
1.45	0.5±0.1	0.45±0.08	0.32±0.05	0.10±0.02	
	0.4±0.1	0.36±0.08	0.26±0.05	0.07±0.02	
1.55	0.4±0.1	0.26±0.06	0.14±0.03	0.07±0.02	
	0.4±0.1	0.28±0.07	0.21±0.04	0.04±0.01	
1.57					0.008±0.002
					0.004±0.002
1.65	0.4±0.1	0.24±0.05	0.10±0.03	0.05±0.01	
	0.12±0.06	0.23±0.06	0.12±0.03	0.04±0.01	

centrality is strongest for kaons, intermediate for (anti)protons, and weakest for pions. This indicates that protons and antiprotons have a larger component scaling with N_{coll} than pions.

We fit the yields per participant with Eq. (21). As in Refs. [62,63] we parametrize the multiplicity using two free parameters: n_{pp}, the multiplicity in $p+p$ collisions, and x, the relative strength of the component scaling with N_{coll}.

$$R \equiv \frac{dN/dy}{N_{\mathrm{part}}} = (1-x)n_{pp}\frac{1}{2} + xn_{pp}\frac{N_{\mathrm{coll}}}{N_{\mathrm{part}}} = n_{pp}\left[\frac{1}{2} + x\left(\frac{N_{\mathrm{coll}}}{N_{\mathrm{part}}} - \frac{1}{2}\right)\right]. \quad (21)$$

The results of the fit are shown as solid lines in Fig. 25. The fit parameter values are given in Table VIII. All hadron spe-

TABLE XII. (Anti)proton invariant yields in each event centrality and p_T bin, measured at midrapidity and normalized to one rapidity unit. The top row in each p_T is the proton yield, and the bottom row the anitproton. The errors are statistical only.

p_T(GeV/c)	0–5 %	5–15 %	15–30 %	30–60 %	60–92 %
0.545					0.26±0.06
					0.12±0.05
0.55	8±1	4.9±0.5	4.0±0.4	1.6±0.2	
	4.2±0.8	2.8±0.5	2.0±0.3	0.8±0.1	
0.65	6.3±0.7	4.7±0.4	2.7±0.2	1.2±0.1	
	4.3±0.7	2.6±0.4	1.9±0.3	0.9±0.1	
0.695					0.14±0.02
					0.14±0.03
0.75	4.4±0.5	4.0±0.4	2.2±0.2	0.90±0.08	
	3.6±0.5	2.5±0.3	1.7±0.2	0.60±0.08	
0.85	3.9±0.4	3.3±0.3	1.9±0.2	0.75±0.07	
	2.9±0.5	2.5±0.3	1.8±0.2	0.62±0.08	
0.895					0.10±0.02
					0.06±0.01
1.00	3.1±0.2	2.4±0.2	1.37±0.09	0.46±0.03	
	2.1±0.2	1.5±0.1	0.91±0.08	0.41±0.04	
1.18					0.031±0.005
					0.018±0.004
1.20	2.0±0.2	1.4±0.1	0.82±0.06	0.28±0.02	
	1.4±0.2	1.0±0.1	0.54±0.05	0.19±0.02	
1.40	1.1±0.1	0.74±0.07	0.46±0.04	0.14±0.01	
	0.9±0.1	0.50±0.06	0.32±0.04	0.13±0.02	
1.58					0.005±0.002
					0.007±0.002
1.60	0.54±0.07	0.49±0.05	0.25±0.03	0.09±0.01	
	0.49±0.08	0.37±0.05	0.20±0.03	0.053±0.009	
1.80	0.34±0.05	0.25±0.03	0.16±0.02	0.047±0.007	
	0.27±0.06	0.11±0.02	0.10±0.02	0.021±0.005	
1.98					0.003±0.001
					0.0005±0.0005
2.00	0.20±0.04	0.12±0.02	0.10±0.01	0.029±0.005	
	0.16±0.04	0.08±0.02	0.05±0.01	0.026±0.006	
2.20	0.13±0.03	0.08±0.02	0.05±0.01	0.008±0.002	
	0.04±0.02	0.03±0.01	0.025±0.007	0.010±0.003	
2.41					0.0010±0.0006
					0.0020±0.0008
2.425	0.06±0.02	0.05±0.01	0.017±0.005	0.007±0.002	
	0.05±0.02	0.04±0.01	0.011±0.004	0.006±0.002	
2.675	0.014±0.008	0.019±0.006	0.010±0.003	0.004±0.001	
	0.005±0.005	0.018±0.007	0.002±0.002	0.0012±0.0008	
2.908					0.0006±0.0004
					0.0005±0.0003
2.925	0.017±0.007	0.006±0.003	0.006±0.002	0.003±0.001	
	0.020±0.009	0.009±0.004	0.003±0.002	0.0009±0.0006	
3.175	0.013±0.006	0.002±0.002	0.003±0.002	0.0012±0.0007	
	0.006±0.004	0.003±0.002	0.0010±0.001		
3.425	0.004±0.003	0.003±0.002	0.002±0.001	0.0007±0.0005	
	0.002±0.002	0.001±0.001	0.002±0.001	0.0003±0.0003	
3.675	0.003±0.003			0.0003±0.003	
	0.003±0.003		0.0008±0.0008		

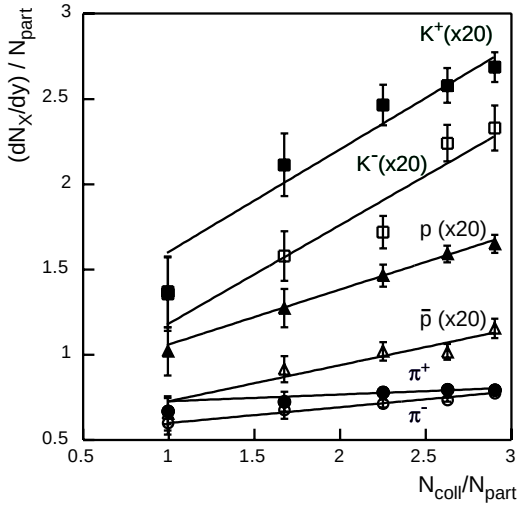

FIG. 25. dN/dy per participant of different particle species as a function of the number of collisions per participant. Kaon and (anti)proton multiplicities are scaled by a factor of 20.

cies are well fit. The importance of the component scaling as N_{coll} is the largest for kaons and smallest for pions.

We check the consistency of the fits in Fig. 25 with known hadron yields in $p+p$ collisions by extrapolating the fits down to two participants (and one binary nucleon-nucleon collision). Isospin differences between $p+p$ and Au+Au are ignored. The check is done by separately extrapolating the fitted fraction of yield which scales with N_{coll} and the fraction scaling with N_{part} down to one nucleon-nucleon collision and two participant nucleons, and summing the result. One obtains particle ratios of $K/\pi=(8.7\pm2.6)\%$ and $\overline{p}/\pi=(4.9\pm0.8)\%$. These values fall between those measured at lower $\sqrt{s}$ at the ISR [67] and those at higher $\sqrt{s}$ at the Tevatron [68], as expected since the RHIC energy lies in-between. Thus the Au+Au data are shown to scale down to $p+p$ reasonably.

One may expect that the particle ratios at very high p_T should be dominated by hard scattering, and therefore scale

TABLE IX. (*Continued.*)

p_T(GeV/c)	$\pi^{\pm}$	$K^{\pm}$	$p(\overline{p})$
	0.020 ± 0.004		
2.30			0.020 ± 0.003
			0.012 ± 0.002
2.50			0.010 ± 0.002
			0.011 ± 0.002
2.70			0.006 ± 0.001
			0.0026 ± 0.0009
2.90			0.0035 ± 0.0008
			0.003 ± 0.001
3.10			0.0028 ± 0.0007
			0.0011 ± 0.0005
3.30			0.0014 ± 0.0005
			0.0010 ± 0.0004

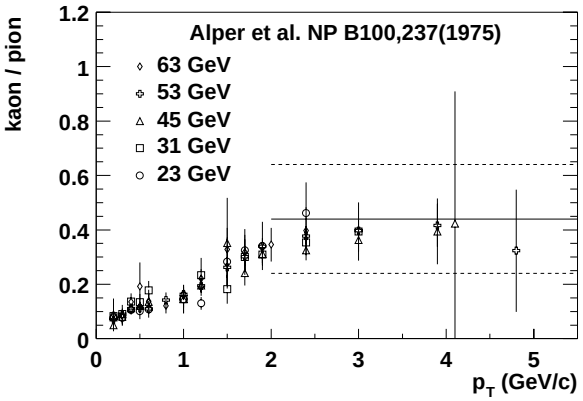

FIG. 26. Kaon to pion ratio as a function of p_T. The different points are measured in $p+p$ collisions (data from Ref. [69]). The solid line is the asymptotic value for high p_T in $p+p$ derived from the hard scattering component of the fits using Eq. (21) to the measured centrality dependence of dN/dy in Au-Au collisions at $\sqrt{s_{NN}}=130$ GeV. The dashed lines indicate the corresponding uncertainty.

with the number of binary collisions. Consequently, we look at ratios of the N_{coll} scaling components alone, extrapolated down to one binary collision. The values are compared to measurements of hadron ratios at the ISR [69] in Figs. 26 and 27. The ratios of the extrapolated Au+Au yield fractions scaling as N_{coll} are shown as solid lines for $p_T\geqslant2$ GeV/c. The agreement with the $p+p$ data at high p_T is quite good.

Finally, we directly compare p/π and $\overline{p}/\pi$ ratios in central Au+Au collisions with $p+p$, as a function of p_T. These ratios from the 10% most central data, using the charged particle measurement from this paper and neutral pions from Ref. [39], are shown in Fig. 28. The ratios show a steady increase up to 2.5 GeV/c in p_T. Even though the simple extrapolation of the N_{coll} scaling yield fraction agreed with $p+p$, the ratios of the full yield significantly exceed those in the ISR measurements [69]. According to Gyulassy and co-

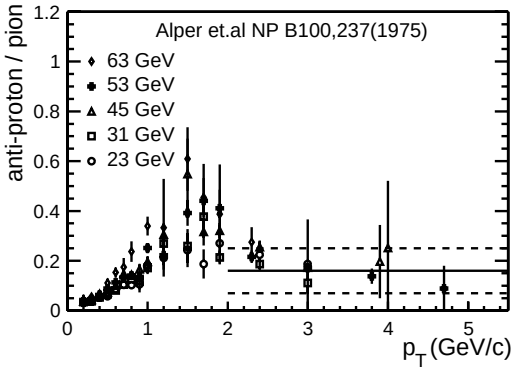

FIG. 27. Antiproton to π^- ratio as a function of p_T. The different points are measured in $p+p$ collisions (data from Ref. [69]). The solid line is the asymptotic value for high p_T in $p+p$ derived from the hard scattering component of the fits using Eq. (21) to the measured centrality dependence of dN/dy in Au-Au collisions at $\sqrt{s_{NN}}=130$ GeV. The dashed lines indicate the corresponding uncertainty.

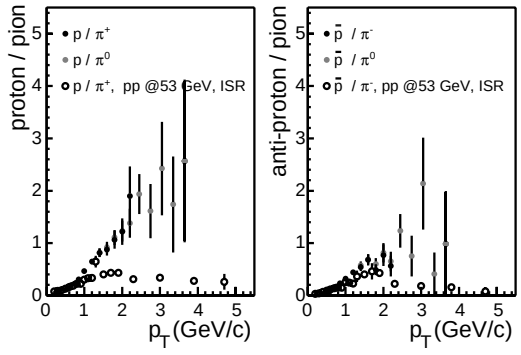

FIG. 28. (a) Proton to pion ratio as a function of p_T. (b) Antiproton to pion ratio as a function of p_T. The open circles represent measurements in $p+p$ collisions (data from Ref. [69]). The filled circles show the 10% most central Au+Au collisions. The neutral pion spectra are from the data published in Ref. [39].

workers [70] this result may give insight into baryon number transport and the interplay between soft and hard processes.

Of course, splitting the observed yields into portions that scale with $N_{\rm part}$ and $N_{\rm coll}$ is by no means a unique explanation of the data. The spectra and yields can also be well reproduced by thermal models, which break such simple scalings due to the multiple interactions suffered by the constituents.

Simple thermal models that ignore transverse and longitudinal flow [71] are able to describe the centrality dependence of the midrapidity $\pi^{\pm}$, $K^{\pm}$, p, and $\overline{p}$ yields by tuning the chemical freeze-out temperature $T_{\rm ch}$, the baryon chemical potential μ_B and by introducing a strangeness saturation factor γ_s. It was found that μ_B is independent of centrality, while both $\gamma_{\rm s}$ and $T_{\rm ch}$ increase from peripheral to central collisions. Within the same model, the centrality dependence of the particle yields at lower energy ($\sqrt{s_{NN}}=17$ GeV [72,73]) are described by constant $T_{\rm ch}$ and μ_B. The strong centrality dependence in kaon production at both energies is accounted for by the increase in the strangeness saturation factor γ_s. Although the integrated particle yields are very well described, such simple thermal models do not attempt a comparison to the single-particle spectra, which clearly indicate centrality dependent flow effects not included in the model.

Thermal models that include hydrodynamical parameters on a freeze-out hypersurface to account for longitudinal and transverse flow can reproduce the absolutely normalized particle spectra by introducing only two thermal parameters $T_{\rm ch}$ and μ_B [74,75]. In this approach, the thermal parameters are independent of centrality, while the geometric parameters are adjusted to reproduce the spectra. Good agreement with the data is obtained up to $p_T \approx 2-3$ GeV/c, however, an explicit comparison with the centrality dependence of the integrated midrapidity yields has not yet been made.

This section shows that the yields of all hadrons increase more rapidly than linearly with the number of participants, but the increase is weaker than scaling with the number of binary collisions. The excess beyond linear scaling with $N_{\rm part}$ is the strongest for kaons, intermediate for (anti)protons, and weakest for pions. The centrality dependence of the total yields can be well fit with a sum of these two kinds of scaling. At high p_T, the baryon and antibaryon yields greatly exceed expectations from $p+p$ collisions. Thermal models, which do not invoke strict scaling rules, can successfully reproduce the data as well, providing that they include the radial flow required by the p_T spectra.

VI. SUMMARY AND CONCLUSION

We have presented the spectra and yields of identified hadrons produced in $\sqrt{s_{NN}}=130$ GeV Au+Au collisions. The yields of pions increase approximately linearly with the number of participant nucleons, while the yield increase is faster than linear for kaons, protons, and antiprotons.

Hydrodynamic analyses of the particle spectra are performed: the spectra are fit with a hydrodynamic-inspired parametrization to extract freeze-out temperature and radial flow velocity of the particle source. The data are also compared to two full hydrodynamics calculations. The simultaneous fits of pion, kaon, proton, and antiproton spectra show that radial flow in central collisions at RHIC exceeds that at lower energies and increases with centrality of the collision. The hydrodynamic models are consistent with the measured spectral shapes, extracted freeze-out temperature $T_{\rm fo}$, and the flow velocity β_T in central collisions.

TABLE XIII. Minimum-bias invariant yields for all particles in equal p_T bins. For each p_T, the first line are the positive particle yields and the second are the negative particle yields. The units are c^2/Gev^2.

p_T(GeV/c)	$\pi^{\pm}$	$K^{\pm}$	(anti)p
0.25	112±2		
	109±2		
0.35	56±1		
	49.9±0.9		
0.45	28.0±0.5	6.1±0.4	
	24.1±0.5	4.6±0.4	
0.55	15.7±0.3	4.0±0.3	2.3±0.1
	14.6±0.3	3.2±0.2	0.38±0.02
0.70	7.3±0.1	2.18±0.09	1.55±0.06
	7.0±0.1	1.9±0.1	1.07±0.06
0.90	3.06±0.06	1.07±0.05	1.08±0.04
	2.89±0.07	0.91±0.05	0.79±0.04
1.20	0.91±0.02	0.38±0.02	0.49±0.02
	0.98±0.02	0.32±0.02	0.35±0.01
1.60	0.208±.007	0.104±0.006	0.157±0.007
	0.193±0.007	0.093±0.006	0.119±0.007
2.00	0.050±0.003		0.051±0.003
	0.053±0.003		0.031±0.003
2.45	0.0028±0.005		0.013±0.001
	0.0034±0.0006		0.009±0.001
2.95			0.0036±0.0006
			0.0022±0.0005
3.55			0.007±0.0002
			0.0006±0.0002

TABLE XIV. Pion invariant yields in each event centrality normalized to one rapidity unit at midrapidity. The first line corresponds to positive pions and the second to negative pions.

p_T(GeV/c)	0–5 %	5–15 %	15–30 %	30–60 %	60–92 %
0.25	355±9	282±6	186±4	81±2	13.2±0.5
	371±10	275±7	180±4	74±2	12.1±0.5
0.35	188±5	146±3	93±2	36.6±0.8	5.3±0.2
	169±5	128±3	82±2	34.3±0.9	5.0±0.2
0.45	95±3	74±2	48±1	17.5±0.5	2.7±0.1
	86±3	63±2	40±1	15.7±0.5	2.1±0.1
0.55	56±2	41±1	26.0±0.7	10.1±0.3	1.32±0.09
	51±2	38±1	24.5±0.8	9.6±0.3	1.18±0.09
0.70	26.3±0.8	20.2±0.5	12.3±0.3	4.4±0.1	0.62±0.04
	24.7±0.9	18.6±0.6	11.8±0.4	4.5±0.1	0.57±0.04
0.90	11.0±0.4	7.9±0.2	5.1±0.2	1.79±0.06	0.19±0.02
	10.0±0.5	7.9±0.3	5.0±0.2	1.76±0.07	0.24±0.02
1.20	3.1±0.1	2.37±0.09	1.50±0.05	0.58±0.02	0.064±0.006
	3.4±0.2	2.7±0.1	1.67±0.07	0.64±0.03	0.061±0.007
1.60	0.62±0.05	0.54±0.03	0.34±0.02	0.142±0.009	0.015±0.003
	0.63±0.06	0.58±0.04	0.32±0.02	0.129±0.009	0.014±0.003
2.00	0.17±0.02	0.14±0.01	0.083±0.009	0.027±0.003	0.005±0.001
	0.20±0.03	0.14±0.02	0.09±0.01	0.035±0.004	0.004±0.001
2.45	0.005±0.003	0.009±0.003	0.006±0.002	0.0017±0.0006	
	0.011±0.005	0.11±0.004	0.005±0.002	0.0025±0.0009	

Extrapolating the fits to estimate thermal particle production at higher p_T allows us to study the soft-hard physics boundary by comparing to measured spectra at high p_T. The yield of the soft protons reaches, and even exceeds, that of the extrapolated soft pions at 2 GeV/c p_T. The sum of the extrapolated soft spectra agrees with the measured inclusive data to $p_T \approx 2.5-3$ GeV/c. The transition from soft to hard processes must be species dependent, and the admixture of boosted nucleons implies that hard processes do not dominate the inclusive charged particle spectra until ≈ 3 GeV/c.

ACKNOWLEDGMENTS

We thank the staff of the RHIC Project, Collider-Accelerator, and Physics Departments at Brookhaven National Laboratory and the staff of the other PHENIX participating institutions for their vital contributions. We acknowledge support from the Department of Energy, Office of Science, Nuclear Physics Division, the National Science Foundation, and Dean of the College of Arts and Sciences, Vanderbilt University (U.S.), Ministry of Education, Culture,

TABLE XV. Kaon invariant yields in each event centrality normalized to one rapidity unit at midrapidity. The first line corresponds to positive kaons and the second to negative kaons.

p_T(GeV/c)	0–5 %	5–15 %	15–30 %	30–60 %	60–92 %
0.45	21±3	16±2	10±1	4.3±0.5	0.5±0.1
	21±3	13±2	7±1	2.5±0.4	0.4±0.1
0.55	15±2	11±1	6.6±0.7	2.4±0.3	0.20±0.07
	13±2	8±1	4.8±0.6	2.3±0.3	0.3±0.1
0.70	8.0±0.7	6.6±0.5	4.3±0.3	1.5±0.1	0.18±0.03
	7.0±0.8	6.5±0.6	3.1±0.3	1.1±0.1	0.14±0.03
0.90	4.5±0.4	3.1±0.2	1.9±0.1	0.62±0.06	0.06±0.02
	3.3±0.4	3.3±0.3	1.6±0.2	0.5±0.06	0.09±0.02
1.20	1.4±0.1	1.10±0.08	0.68±0.05	0.22±0.02	0.012±0.004
	1.3±0.1	0.97±0.08	0.50±0.05	0.17±0.02	0.015±0.005
1.60	0.36±0.05	0.29±0.03	0.17±0.02	0.062±0.007	0.008±0.002
	0.29±0.05	0.27±0.03	0.20±0.02	0.058±0.008	0.004±0.002

TABLE XVI. (Anti)proton invariant yields in each event centrality normalized to one rapidity unit at midrapidity. The first line corresponds to protons and the second to antiprotons.

p_T(GeV/c)	0–5 %	5–15 %	15–30 %	30–60 %	60–92 %
0.55	8±1	4.9±0.5	4.0±0.4	1.6±0.2	0.26±0.06
	4.2±0.8	2.8±0.5	2.0±0.3	0.8±0.1	0.12±0.05
0.70	5.4±0.4	4.5±0.3	2.5±0.2	1.06±0.07	0.14±0.02
	4.4±0.5	2.9±0.3	2.0±0.2	0.80±0.08	0.14±0.03
0.90	3.9±0.3	3.1±0.2	1.9±0.1	0.71±0.05	0.10±0.02
	2.8±0.3	2.1±0.2	1.4±0.1	0.58±0.05	0.06±0.01
1.20	1.9±0.1	1.37±0.08	0.78±0.04	0.26±0.02	0.031±0.005
	1.3±0.1	0.96±0.07	0.56±0.04	0.21±0.02	0.018±0.004
1.60	0.60±0.06	0.44±0.03	0.27±0.02	0.087±0.008	0.005±0.002
	0.49±0.06	0.34±0.03	0.19±0.02	0.062±0.007	0.007±0.002
2.00	0.20±0.03	0.15±0.02	0.09±0.01	0.025±0.003	0.003±0.001
	0.15±0.03	0.07±0.01	0.055±0.009	0.019±0.003	0.0005±0.0005
2.45	0.06±0.01	0.040±0.007	0.020±0.004	0.006±0.001	0.0010±0.0006
	0.04±0.01	0.028±0.006	0.011±0.003	0.005±0.001	0.0020±0.0008
2.95	0.015±0.005	0.007±0.002	0.005±0.002	0.0023±0.0007	0.0006±0.0004
	0.013±0.005	0.008±0.003	0.002±0.007	0.0003±0.0003	0.0005±0.0003
3.55	0.003±0.002	0.0012±0.007	0.0014±0.006	0.0005±0.0002	
	0.002±0.001	0.0011±0.007	0.0013±0.006	0.0002±0.0002	

Sports, Science, and Technology and the Japan Society for the Promotion of Science (Japan), Russian Academy of Science, Ministry of Atomic Energy of Russian Federation, Ministry of Industry, Science, and Technologies of Russian Federation (Russia), Bundesministerium für Bildung und Forschung, Deutscher Akademischer Auslandsdienst, and Alexander von Humboldt Stiftung (Germany), VR and the Wallenberg Foundation (Sweden), MIST and the Natural Sciences and Engineering Research Council (Canada), Conselho Nacional de Desenvolvimento Científico e Tecnológico and Fundação de Amparo à Pesquisa do Estado de São Paulo (Brazil), Natural Science Foundation of China (People's Republic of China), Centre National de la Recherche Scientifique, Commissariat à l'Énergie Atomique, Institut National de Physique Nucláire et de Physique des Particules, and Association pour la Recherche et le Développement des Méthodes et Processus Industriels (France), Department of Atomic Energy and Department of Science and Technology (India), Israel Science Foundation (Israel), Korea Research Foundation and Center for High Energy Physics (Korea), the U.S. Civilian Research and Development Foundation for the Independent States of the Former Soviet Union, and the U.S.-Israel Binational Science Foundation.

APPENDIX A: DETERMINING N_{part} AND N_{coll}

As only the fraction of the total cross section is measured in both ZDC and BBC detectors, a model-dependent calculation is used to map collision centrality to the number of participant nucleons, N_{part}, and the number of binary nucleon-nucleon collisions, N_{coll}. A discussion of this calculation at RHIC can be found elsewhere [62].

Using a Glauber model combined with a simulation of the BBC and ZDC responses, N_{part} and N_{coll} are determined in each centrality. The model provides the thickness of nuclear matter in the direct path of each oncoming nucleon, and uses the inelastic nucleon-nucleon cross section $\sigma_{N+N}^{\mathrm{inel}}$ to determine whether or not a nucleon-nucleon collision occurs. We assume the following.

(1) The nucleons travel in straight-line paths, parallel to the velocity of its respective nucleus.

(2) An inelastic collision occurs if the relative distance between two nucleons is less than $\sqrt{\sigma_{N+N}^{\mathrm{inel}}/\pi}$.

(3) Fluctuations are introduced by using the simulated detector response for both ZDC and BBC.

In this calculation, the Woods-Saxon nuclear density distribution $[\rho(r)]$ is used for each nucleus with two parameters, the nuclear radius $R=6.38^{+0.27}_{-0.13}$ fm and diffusivity $d=0.53\pm0.01$ fm [16]. The central density ρ_0 is determined by normalization to the correct number of nucleons. The inelastic nucleon-nucleon cross section is $\sigma_{N+N}^{\mathrm{inel}}=40\pm3$ mb,

$$\rho(r)=\frac{\rho_0}{1+e^{(r-r_n)/d}}. \tag{A1}$$

APPENDIX B: INVARIANT YIELDS

Tabulated here are the measured invariant yields of pions, kaons, and (anti)protons produced in Au+Au collisions at 130 GeV. Tables IX–XII show the invariant yields plotted in Figs. 9 and 10. Tables XIII–XVI show the invariant yields in equal p_T bins as used in Fig. 11.

APPENDIX C: FREEZE-OUT SURFACE ASSUMPTIONS

The freeze-out surface is $\sigma(r,\phi,\eta)$, where the radius r is between zero and R, the radius at freeze-out, the azimuthal

angle ϕ is between zero and 2π, and the longitudinal space-time rapidity variable η varies between $-\eta_{\max}$ and $\eta_{\max}$. In the Bjorken scenario, the freeze-out surface in space-time is hyperbolic, with contours of constant proper time $\tau = \sqrt{t^2 - z^2}$. Assuming instantaneous freeze-out in the radial direction and longitudinal boost invariance, the model dependence factors out of Eq. (17) and is included in the normalization constant A.

At 130 GeV, the PHOBOS experiment measures the total charged particle pseudorapidity distribution to be flat over 2 units of pseudorapidity [43]. The measured rapidity in PHOBOS is taken to be the same as the rapidity of the fireball, defined here as z. The rapidity variables in the integrand vanish for $|z| > 2$. Therefore, the integration over the fireball rapidity is generally taken to be from $-\infty$ to $+\infty$ using the modified K_1 Bessel function

$$K_1(m_T/T) = \int_0^\infty \cosh(z) e^{-m_T \cosh(z)/T} dz, \qquad \text{(C1)}$$

where the variable z is the fireball rapidity variable. The K_1 bessel function can also result by integration over the measured rapidity y with the assumption that the freeze-out is instantaneous in the radial direction. In this case, no assumption is made on the shape of the freeze-out hypersurface. This also assumes that the total rapidity distribution is measured in the detector. What results is the single differential $1/m_T\, dN/dm_T$ [76].

[1] B. Andersson *et al.*, Phys. Rep. **97**, 31 (1983).
[2] X. Artru, Phys. Rep. **97**, 147 (1983).
[3] J. Owens *et al.*, Phys. Rev. D **18**, 1501 (1978).
[4] K. Ackermann *et al.*, Phys. Rev. Lett. **86**, 402 (2001).
[5] C. Adler *et al.*, Phys. Rev. Lett. **87**, 182301 (2001).
[6] C. Adler *et al.*, Phys. Rev. C **66**, 034904 (2002).
[7] C. Adler *et al.*, Phys. Rev. Lett. **90**, 032301 (2003).
[8] K. Adcox *et al.*, Phys. Rev. Lett. **89**, 212301 (2002).
[9] B. Back *et al.*, Phys. Rev. Lett. **89**, 222301 (2002).
[10] D. Morrison *et al.*, Nucl. Phys. **A638**, 565c (1998).
[11] W. Zajc, Nucl. Phys. **A98**, 39 (2002).
[12] K. Adcox *et al.*, Nucl. Instrum. Methods Phys. Res. A **499**, 469 (2003).
[13] J. Mitchell *et al.*, Nucl. Instrum. Methods Phys. Res. A **482**, 491 (2002).
[14] D. Ben-Tzvi and M. Sandler, Pattern Recogn. Lett. **11**, 167 (1990).
[15] C. Adler *et al.*, Nucl. Instrum. Methods Phys. Res. A **470**, 488 (2001).
[16] R. Glauber and J. Natthiae, Nucl. Phys. **B21**, 135 (1970).
[17] B. Hahn, D. Ravenhall, and R. Hofstadter, Phys. Rev. **101**, 1131 (1956).
[18] S. J. Pollock *et al.*, Phys. Rev. C **46**, 2587 (1992).
[19] D. Groom, Eur. Phys. J. C **3**, 144 (1998).
[20] R. Brun, R. Hagelberg, N. Hansroul, and J. Lassalle, CERN-DD-78-2, 1978.
[21] J. M. Burward-Hoy, Ph.D. thesis, State University of New York at Stony Brook, 2001.
[22] K. Adcox *et al.*, Phys. Rev. Lett. **88**, 242301 (2002).
[23] R. Albrecht *et al.*, Eur. Phys. J. C **5**, 255 (1998).
[24] M. Aggarwal *et al.*, Eur. Phys. J. C **23**, 225 (2002).
[25] M. Faessler, Phys. Rep. **115**, 1 (1984).
[26] K. Adcox *et al.*, Phys. Rev. Lett. **89**, 092302 (2002).
[27] K. Adcox *et al.*, Phys. Rev. Lett. **86**, 3500 (2001).
[28] I. Bearden *et al.*, Phys. Rev. Lett. **78**, 2080 (1997).
[29] H. Boggild *et al.*, Phys. Rev. C **59**, 328 (1999).
[30] I. Bearden *et al.*, Phys. Rev. C **57**, 837 (1998).
[31] I. Bearden *et al.*, Phys. Lett. B **388**, 431 (1996).
[32] E. Andersen, J. Phys. G **25**, 171 (1999).
[33] F. Antinori *et al.*, Phys. Lett. B **433**, 209 (1998).
[34] B. Alper *et al.*, Nucl. Phys. **B100**, 237 (1975).
[35] K. Guettler *et al.*, Nucl. Phys. **B116**, 77 (1976).
[36] B. Alper *et al.*, Nucl. Phys. **B87**, 19 (1975).
[37] K. Guettler *et al.*, Nucl. Phys. **B116**, 77 (1976).
[38] J. Schaffner-Bielich, D. Kharzeev, L. McLerran, and R. Venugopalan, Nucl. Phys. **A705**, 494 (2002).
[39] K. Adcox *et al.*, Phys. Rev. Lett. **88**, 022301 (2002).
[40] B. Back *et al.*, PHOBOS Collaboration, Phys. Rev. C **65**, 061901(R) (2002).
[41] C. Adler *et al.*, STAR Collaboration, Phys. Rev. Lett. **87**, 112303 (2001).
[42] K. Adcox *et al.*, PHENIX Collaboration, Phys. Rev. Lett. **86**, 3500 (2001).
[43] B. Back *et al.*, Phys. Rev. Lett. **85**, 3100 (2000).
[44] E. Schnedermann, J. Sollfrank, and U. Heinz, Phys. Rev. C **48**, 2462 (1993).
[45] S. Esumi, S. Chapman, H. van Hecke, and N. Xu, Phys. Rev. C **55**, R2163 (1997).
[46] M. van Leeuwen for the NA49 Collaboration, Nucl. Phys. **A715**, 161 (2003).
[47] S. Afanasiev *et al.*, Eur. Phys. J. C **2**, 661 (1998).
[48] P. Kolb, Ph.D. thesis, University of Regensburg, 2001.
[49] J. Sollfrank, P. Koch, and U. Heinz, Phys. Lett. B **252**, 256 (1990).
[50] J. Barette *et al.*, Phys. Lett. B **351**, 93 (1995).
[51] H. Boggild *et al.*, Z. Phys. C **69**, 621 (1996).
[52] U. Wiedemann and U. Heinz, Phys. Rev. C **56**, 3265 (1997).
[53] P. Braun-Munzinger, D. Magestro, K. Redlich, and J. Stachel, Phys. Lett. B **518**, 41 (2001).
[54] P. F. Kolb (unpublished).
[55] P. F. Kolb, J. Sollfrank, and U. Heinz, Phys. Rev. C **62**, 054909 (2000).
[56] P. Kolb, P. Huovinen, U. Heinz, and H. Heiselberg, Phys. Lett. B **500**, 232 (2001).
[57] D. Teaney, Ph.D. thesis, State University of New York at Stony Brook, 2001.
[58] D. Teaney, J. Lauret, and E. Shuryak, Phys. Rev. Lett. **86**, 4783 (2001).
[59] H. Sorge, Phys. Rev. C **52**, 3291 (1995).
[60] D. Teaney, J. Lauret, and E. Shuryak, nucl-th/0110037.
[61] W. Broniowski and W. Florkowski, Phys. Rev. Lett. **87**, 272302 (2001).

[62] D. Kharzeev and M. Nardi, Phys. Lett. B **507**, 121 (2001).
[63] X.-N. Wang and M. Gyulassy, Phys. Rev. Lett. **86**, 3496 (2001).
[64] F. Becattini and U. Heinz, Z. Phys. C **76**, 269 (1997).
[65] F. Becattini, Eur. Phys. J. C **5**, 143 (1998).
[66] A. Tounsi and K. Redlich, J. Phys. G **28**, 1761 (2002).
[67] B. Alper *et al.*, Nucl. Phys. **B87**, 19 (1975).
[68] T. Alexopoulos *et al.*, Phys. Rev. D **48**, 984 (1993).
[69] B. Alper *et al.*, Nucl. Phys. **B100**, 237 (1975).
[70] I. Vitev and M. Gyulassy, Phys. Rev. C **65**, 041902 (2002).
[71] B. Kampfer, J. Cleymans, K. Gallmeister, and S. M. Wheaton, Heavy Ion Phys. **18**, 1 (2003).
[72] F. Sikler, Nucl. Phys. **A661**, 45c (1999).
[73] V. Freise, for the NA49 Collaboration, Proceedings of Strangeness in Quark Matter 2003, nucl-ex/0305017, J. Phys. G (to be published).
[74] W. Broniowski, A. Baran, and W. Florkowski, Acta Phys. Pol. B **33**, 4235 (2002).
[75] W. Broniowski and W. Florkowski, Acta Phys. Pol. B **33**, 1629 (2002).
[76] U. Heinz (private communication).